運輸省港湾技術研究所

# 港湾技術研究所報告

# REPORT OF THE PORT AND HARBOUR RESEARCH INSTITUTE

MINISTRY OF TRANSPORT

VOL. 23 NO. 4 DEC. 1984

NAGASE, YOKOSUKA, JAPAN

# 港湾技術研究所報告 (REPORT OF P.H.R.I.)

第23巻　第4号 (Vol. 23, No. 4) 1984年12月 (Dec. 1984)


## 目　　次 (CONTENTS)

REPORT OF THE PORT AND
HARBOUR RESEARCH INSTITUTE
Vol. 23, No. 4 (Dec. 1984)

# 1. Effects of Wind Shear and Waves on the Structure of Turbulent Streams

Hiroichi TSURUYA*
Hiroya TERAKAWA**
Yoshikuni MATSUNOBU***

## Synopsis

Interaction of wind shear or waves and a current was investigated in a wind-wave tank. In the experiment V-type wedge shaped hot-film anemometer was used in order to measure the turbulent fluctuations in longitudinal and vertical components simultaneously. Modification of mean current, characteristic properties of turbulent motions and diffusion coefficients have been discussed.

When wind blows on adverse current, turbulent fluctuations and diffusion coefficient increase near the water surface. On the contraly, near the middle of the flow, they decrease compared with the case of current only. This is closely related to the mean velocity distribution.

In the case that only wind shear acts on the water surface and there are no waves, the way how to predict the turbulent intensities and diffusion coefficient have been proposed.

Under the adverse current condition, turbulent structures which originate in wave-current interaction was investigated. Irregular waves were generated by a plunger type wave maker. Flow velocity was measured with the laser-Doppler anemometer and mean velocity distributions for regular waves in adverse current were discussed with the finite-amplitude wave theory. Frequency response functions for irregular waves propagating on a current were derived. From the experimental data it was confirmed that the linear theory between surface elevations and orbital velocities can hold only near the peak frequency of the waves.

Finally, diffusion of small particles (mixture of chlorobenzene and xylene) in the field where waves and a current coexist was investigated. It became evident that diffusion coefficient in the flow direction increase when waves propagate against the current, but in the vertical direction it does not increase remarkably.

* Chief of Hydrodynamics Laboratory, Marine Hydrodynamics Division
** Formaly, Member of Hydrodynamics Laboratory, Marine Hydrodynamics Division
*** Member of Hydrodynamics Laboratory, Marine Hydrodynamics Division

港湾技術研究所報告
第23巻 第4号 (1984.12)

# 1. 流れの乱れに及ぼす風と波の効果

鶴谷広一*・寺川博也**・松延嘉國***

## 要　旨

風のせん断力あるいは波が作用したときの流れの乱流構造と拡散係数の変化について，大型の風洞水路（幅1.5m，高さ1.3m，全長58.5m）を用いて検討した。流れの乱れはV型のホットフィルム流速計で$x$，$z$成分を同時に測定した。水中に界面活性剤を投入して風波の発生を抑制した実験では，風のせん断力の作用によって水面の近くでは乱れ強度と拡散係数の値が流れだけの場合と比べて20倍程度大きくなることがわかった。しかし，さらに下方の流れの中心部付近では乱れ強度も拡散係数も，流れのみの場合と比べて小さくなった。これは，風のせん断力によって流速分布が変化し，速度勾配と関連した乱れエネルギーの発生の分布に変化が生じたためであることが示された。次に，波と流れの相互干渉の実験では規則波と不規則波が用いられ，逆流上を波が進行する場合の波の減衰，不規則波のスペクトルと統計的性質の変化及び乱れの変化等が検討された。

また，中立粒子を用いた拡散実験を行い，逆流の条件では波形勾配が大きくなると，流れ方向の拡散係数が大きくなり，鉛直方向の拡散係数はほとんど変化しないことが示された。

* 海洋水理部　水理研究室長
** 前海洋水理部　水理研究室（現第三港湾建設局　境港工事事務所）
*** 海洋水理部　水理研究室

## Contents

## 1. Introduction

Turbulence plays an important role in the transport processes in the ocean. Energy, mass and momentum are transported across the air-sea interface which is exposed to the wind shear and surface waves. In the ocean, turbulence is produced both directly from the interfacial stress by the wind and indirectly by the rate of momentum loss from the surface waves by such process as wave breaking (*Phillips*, 1977, p. 256).

In the coastal region, currents such as tidal currents, local wind-generated currents and wave-generated currents are usually observed. Interaction of waves or wind shear and currents is important in many applications. Deformation of surface waves by currents has been investigated by many researchers (e.g., see *Peregrine and Jonsson*, 1983). On the contrary, turbulence of the water flow interacting with waves or wind shear has not been studied sufficiently. A few experimental investigashear and currents is important in many applications. Deformation of surface tions have been made on the alteration of the mean and turbulent flow parameters due to the wave interactions (e.g., see *van Hoften and Karaki*, 1976; *Kemp and Simons*, 1982, 1983). As far as we know, however, no study has been made on the turbulent structure of currents under the action of wind shear.

This paper describes an experimental program carried out in a laboratory wind-wave tunnel, to investigate the interaction between wind shear or gravity waves and a turbulent current. In particular, changes induced in the mean velocity profiles, turbulent intensities and spectra, and diffusion coefficient due to the interaction are investigated.

## 2. General Description of Experiments

The experiments were conducted in a wind-wave tunnel, whose sketches are shown in Figs. 1(a) and 1(b). The dimensions of the test section are 2850 cm long, 150 cm wide, 130 cm deep. The side walls consist of glass plates. A wind blower is located on the windward side (right hand) of the test section over the waterway, and wind is generated by an axial fan driven by a 50 kW variable speed motor. The wind tunnel is fitted with guide vanes, a fine mesh screen and honeycombs in order to provide uniform velocity profiles. The wind speed is set up by regulating the rotational speed (rpm) of the fan. The maximum wind velocity is nearly 30 m/s for the water depth of 50 cm.

The water currents are generated by a pump and a pipeline system. Current direction in the flume can be controlled by the operation of valves. In the present experiments the current condition in each run was controlled by adjusting the flow rate accurately by means of a venturi-meter and a manometer. If the reading of the differential pressure head of manometer exceed $\pm$ 1 mm from the setting value, the flow rate was readjusted.

On the leeward of the uniform test section, an enlarged part is fitted in order to diffuse winds. In this part wooden walls are installed. The width between them is 150 cm, the same as that of the test section. In this part a plunger-type irregular wave maker is installed. This is controlled by a low-inertia DC motor (0.77 kW), the movement of which is directly proportional to the input signal supplied from the

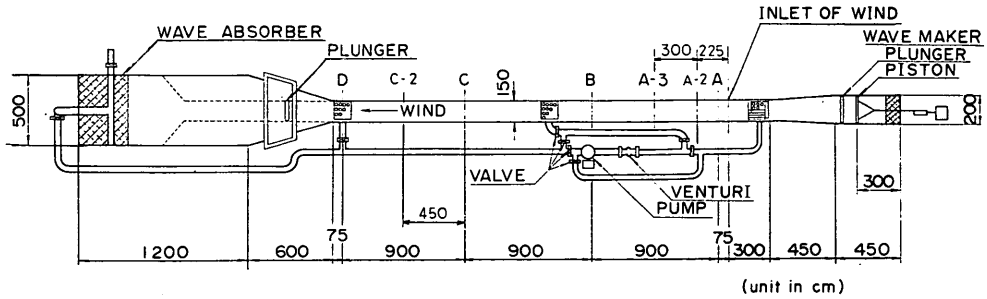


**Fig. 1 (a)**

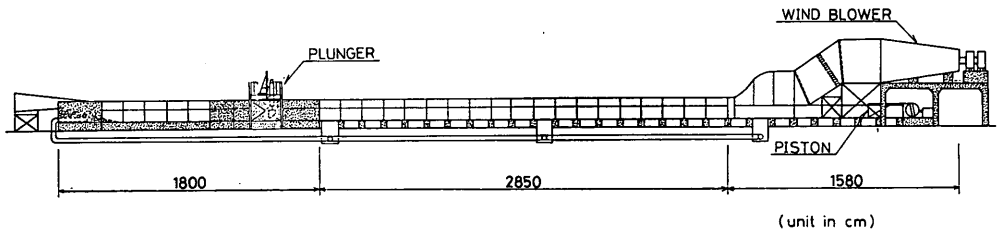


**Fig. 1 (b)**

**Fig. 1** Wind-Wave Tunnel

analog data recorder. The maximum wave height is 10 cm in the case of wave period of 1.0 s. At the windward end of the channel, a piston-type wave maker is equipped to generate regular waves of relatively long period.

Measurements were made in the experiments at the stations A, A-2, A-3, B, C, and D. The fetches at these stations were 0.75, 2.25, 5.25, 9.75, 18.75 and 27.75 m, respectively.

## 3. Turbulence Structure and Diffusion Coefficient of Streams under the Action of Wind

### 3.1 Experimental Equipments and Procedures

The characteristics of the turbulent motion and the diffusion coefficients are much complicated in the situation where wind waves and currents both exist. In order to simplify the phenomenon and to examine the contributions of wind shear alone to the mean velocity distribution, turbulent motion and the diffusion coefficient, the present series of experiments were conducted with wind waves being suppressed.

Some detergent was applied to the water in order to suppress the generation of wind waves. By a preliminary test, it was confirmed that 1.8 kg of detergent was sufficient to suppress the wind waves in the flume. In this condition the concentration of the detergent was 24.5 ppm. It was decided to keep the water depth at the measuring section constant at 45 cm.

The revolutions of the wind blower was kept constant of 300 rpm. In this case the free stream wind velocity near the inlet of wind was 8.1 m/s. Wind velocities over the water surface were measured with a pitot static tube and a MKS BARATRON type 310BH differential pressure head and type 170M-6B electronic

unit. The mean water flow velocity was set at 23.8 and 30.3 cm/s. Measurements of current velocity were made with a DISA type 55R72 wedge-shaped V-type hot-film anemometer at various elevations at the station A and B. The anemometer was operated at an overheat ratio of 1.05. It was calibrated by towing it at constant speed within still water in a calibration tank. The carriage speed was determined by measuring the time that it took to traverse a 1 m length of the tank. In the experiment the V-probe was attached to a self-elevating system which could be raised and lowered a distance of 110 cm with an setting accuracy of 0.1 mm. The probe was carefully cleaned by using a small brush before each measurement. The effective fetches of the stations A and B were 0.75 and 9.75 m, respectively. The experimental conditions are summerized in Table 1.

**Table 1** Experimental Conditions

| Case | Station | $U_a$ (m/s) | $\overline{U}_w$ (cm/s) |
|---|---|---|---|
| S-1 | A | 8.1 | 23.8 |
| S-2 | | | 30.3 |
| S-3 | B | | 23.8 |

The surface drift current velocity was calculated by measuring the time of floats passing two stations 30 cm upwind and downwind from the test section respectively. Thin circular papers of 0.56 cm diameter punched from computer cards, saturated with paraffin, were used as surface floats.

A digital data recorder (DATAC-2000B, Iwatsu Electronic Co., Ltd.) was used for recording the output signals from the measuring instruments on the on-line basis. The sampling time interval of turbulent velocities was usually $\Delta t=1/102.4$ s and the total data number $N=16384$. Some of the data were sampled at $\Delta t=1/204.8$ s and the total data number $N=32768$. Consequently the time of measurement in both cases were 160 s exactly.

### 3.2 Wind Velocity Profile

Figure 2 shows the wind velocity profiles at stations from A to D. The fetch of each stations is represented in Chapter 2.

The mean velocity profiles near the air-water interface follow a logarithmic distribution

$$U_a(z)=\frac{u_{*a}}{\kappa}\ln\frac{z}{z_{0a}}, \tag{3.1}$$

where $U_a(z)$ is the wind velocity at an elevation $z$ above the mean water surface, $u_{*a}$ $(=\sqrt{\tau_a/\rho_a})$ the friction velocity of the wind, $\tau_a$ wind shear stress at the water surface, $\rho_a$ the density of air, $\kappa$ the von Karman constant usually taken to be 0.4 and $z_{0a}$ the roughness length.

Generally, shear stress $\tau$ in the fluid is related to the friction velocity $u_*$ by the following relation

$$\tau=\rho u_*^2, \tag{3.2}$$

where $\rho$ is the density of the fluid. As it has been well confirmed that the velocity

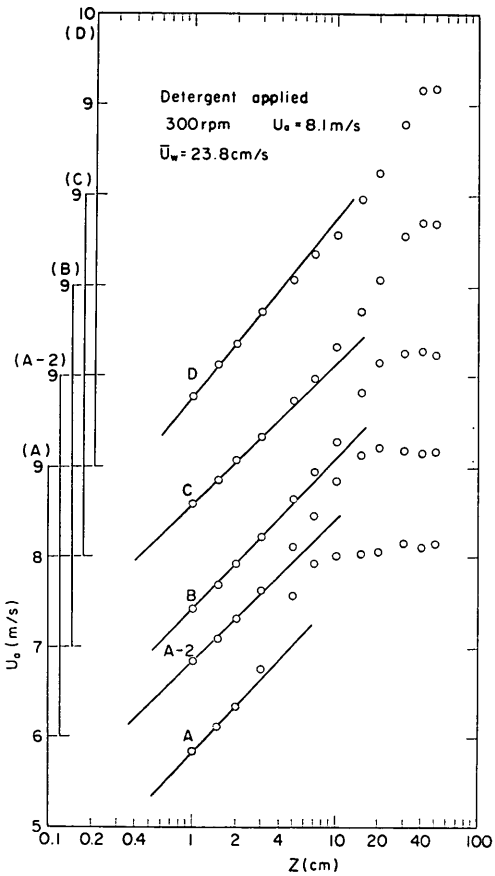


**Fig. 2** Wind Profiles over the Water Surface. Abscissa is Shifted Successively for Different Fetches

distribution near the wall or water surface follow the logarithmic distribution as shown by Eq. (3.1), we can estimate the friction velocity $u_*$ by applying Eq. (3.1) to the measured data. In the same way as the air flow over the water surface, we can define the friction velocities $u_{*w}$ and $u_{*b}$ for the water flow at the water surface and the bed, respectively.

The friction velocities $u_{*a}$ were estimated by applying Eq. (3.1) to the measured data. They are 29.2, 27.8, 29.0, 27.1 and 34.3 cm/s for the stations A, A-2, B, C and D, respectively. The roughness parameter $z_{0a}$ and eddy viscosity $\nu_a$ of the wind are $2.946 \times 10^{-4}$ cm and 0.148 cm$^2$/s at the station A.

### 3.3 Current Velocity Distribution

Mean velocity distributions of currents with and without wind are shown in Figs. 3, 4 and 5. They correspond to the cases S-1, S-2 and S-3, respectively and the experimental conditions have already been shown in Table 1. In order to examine the influence of detergent to the mean velocity distribution, velocity measurements without wind were made for both with and without detergent (Fig. 3). Although there is some scatter in the case of detergent applied, no significant effect can be

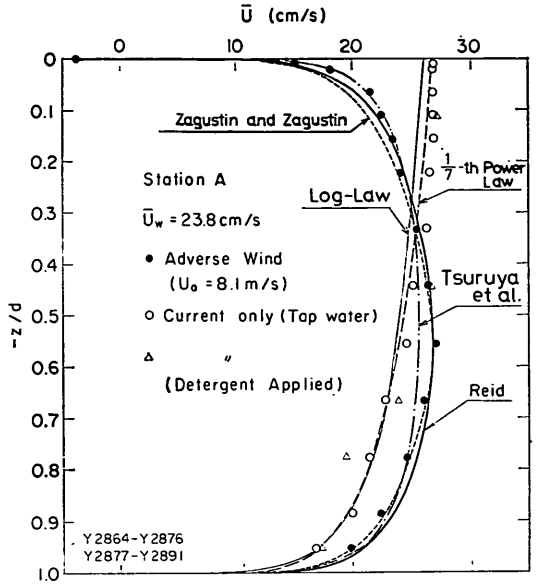


**Fig. 3** Current Profiles (Station A, $\bar{U}_w$=23.8 cm/s)

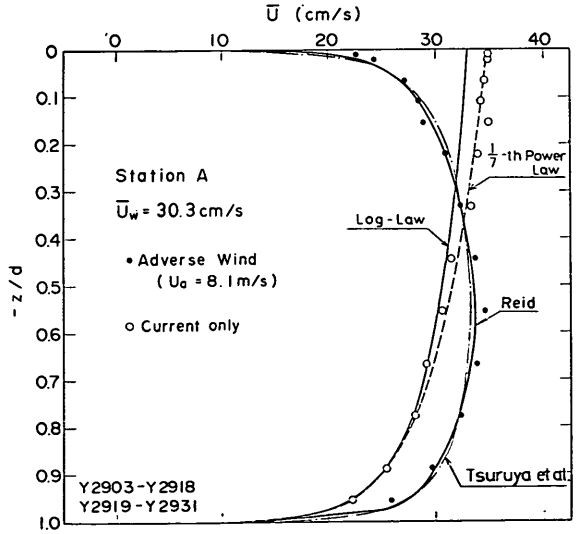


**Fig. 4** Current Profiles (Station A, $\bar{U}_w$=30.3 cm/s)

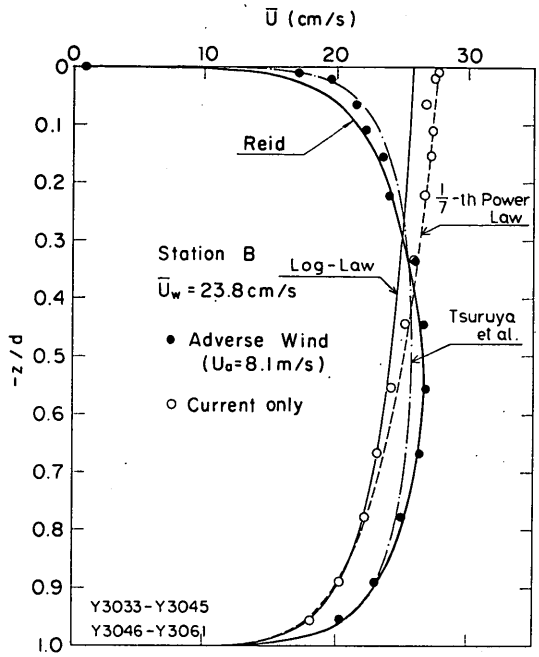


**Fig. 5** Current Profiles (Station B, $\bar{U}_w = 23.8$ cm/s)

found.

In open-channel flow, the well known velocity distributions are logarithmic and 1/7-th power laws. Logarithmic law has the same form as Eq. (3.1) and the mean velocity distribution for open-channel flow can be expressed as

$$\bar{U}(z)=\frac{u_{*b}}{\kappa}\ln\frac{z+a}{z_{0b}}, \tag{3.3}$$

where $\bar{U}(z)$ is the mean velocity at an elevation $z$, $u_{*b}$ the friction velocity at the bottom, $z_{0b}$ the roughness length at the bed and $d$ the depth of water. Friction velocity and the roughness length were estimated from the observed velocity distribution near the bed. The relation (3.3) is represented in Figs. 3, 4 and 5. As the value of $-z/d$ decreases (in the upper layer of the flow), the difference between the experimental data and Eq. (3.3) becomes remarkable.

The 1/7-th power law is

$$\bar{U}(z)=u_0\left(\frac{z+d}{d}\right)^{\frac{1}{7}}, \tag{3.4}$$

where $u_0$ is the water surface velocity. Equation (3.4) is represented as a broken line. For all cases the agreement is better than the logarithmic distribution.

The velocity distribution in an open-channel turbulent flow in the presence of a surface wind stress has been investigated by *Reid* (1957) and *Tsuruya et al.* (1983). The theories will be explained in order.

*Reid* (1957) derived the generalized formula for velocity profile which takes the influence of surface stress into account making use of *Montgomery's* (1943) generali-

zation of the *Prandtl–von Karman's* mixing length theory. Its theoretical derivation is outlined below.

According to *Prandtl's* one-dimensional mixing-length theory (e.g., see *Hinze* 1975, p. 364), the shear stress at the elevation $z$ can be represented as follows

$$\tau=\rho_w l^2 \left|\frac{d\bar{U}(z)}{dz}\right| \frac{d\bar{U}(z)}{dz}, \tag{3.5}$$

where $\rho_w$ is the density of water and $l$ the mixing length.

For the case of flow in a wide channel with a free surface, the generalized mixing length hypothesis of *Montgomery* (1943) leads to the following quadratic from for the mixing length

$$l=\frac{\kappa}{d}(d+z+z_{0b})(z_{0w}-z), \tag{3.6}$$

where $z_{0b}$ is a characteristic roughness length for the channel bed and $z_{0w}$ is a similar characteristic parameter for the free surface. Near the surface and the bottom Eq. (3.6) reduces to the well known relation $l=\kappa z$.

Next, the shear stress within the flow is assumed to have a linear distribution. If $\tau_s$ is the shear stress at the free surface and $\tau_b$ the bottom stress, the shear stress $\tau$ can be represented as

$$\tau=\tau_s\frac{d+z}{d}-\tau_b\frac{z}{d}, \tag{3.7}$$

in which $x$ axis is taken to the direction of $\tau_s$. The velocity distribution for the adverse current condition can be obtained by integrating Eq. (3.5) making use of Eqs. (3.6) and (3.7) as

$$\frac{\bar{U}(z)}{u_{*w}}=-U_m-\frac{1}{\kappa'}\left[B_0\ln\frac{B_0-y}{B_0+y}+2B_1\tan^{-1}\frac{y}{B_1}\right], \quad \zeta<\zeta_m, \tag{3.8}$$

$$\frac{\bar{U}(z)}{u_{*w}}=-U_m-\frac{1}{\kappa'}\left[2B_0\tan^{-1}\frac{y}{B_1}+B_1\ln\frac{B_1-y}{B_1+y}\right], \quad \zeta>\zeta_m, \tag{3.9}$$

$$U_m=\frac{1}{k'}\left[B_0\ln\frac{B_0+\sqrt{|m|}}{B_0-\sqrt{|m|}}-2B_1\tan^{-1}\frac{\sqrt{|m|}}{B_1}\right], \tag{3.10}$$

$$\begin{aligned}
&m=\frac{\tau_b}{\tau_s},\\
&\zeta=\frac{d+z}{d},\\
&\zeta_m=\frac{|m|}{1+|m|},\\
&y=\sqrt{|m+(1-m)\zeta|},\\
&B_0=\sqrt{|(1-m)r_0-m|},\\
&B_1=\sqrt{|1+(1-m)r_1|},\\
&\kappa'=\kappa(1+r_0+r_1),\\
&r_0=\frac{z_{0b}}{d},
\end{aligned} \tag{3.11}$$

$$r_1=\frac{z_{0w}}{d},$$

where $u_{*w}$ is the friction velocity of the water flow at the free surface, $\tau_s$ $(=\rho_w u_{*w}^2)$ the shear stress at the water surface and $\tau_b$ is the shear stress at the bed.

If $r_0$, $r_1 \ll 1$ and $m<0$ the surface velocity $u_0$ can be approximated from Eq. (3.9), namely,

$$\frac{u_0}{u_{*w}}=\frac{1}{\kappa}\left[\ln\frac{4}{(1+|m|)r_1}+2\tan^{-1}\sqrt{|m|}-\sqrt{|m|}\left\{\ln\frac{4|m|}{(1+|m|)r_0}+2\tan^{-1}\frac{1}{\sqrt{|m|}}\right\}\right]. \tag{3.12}$$

The mean current velocity $\bar{U}_w$ is defined as

$$\bar{U}_w=\frac{1}{d}\int_{-d}^{0}\bar{U}(z)dz. \tag{3.13}$$

The substitution of Eqs. (3.8) and (3.9) in the integral of Eq. (3.13) leads to

$$\frac{\bar{U}_w}{u_{*w}}=\frac{2}{\kappa}\left[1+\sqrt{|m|}-B_0\left\{\tan^{-1}\frac{1}{B_0}+\frac{1}{2}\ln\frac{B_0+\sqrt{|m|}}{B_0-\sqrt{|m|}}\right\}\right]. \tag{3.14}$$

If the mean velocity is specified for the given $m$ and $\tau_s$, the bed roughness length $z_{0b}$ can be obtained from Eq. (3.14). The parameters employed in calculating Eqs. (3.8) and (3.9) are summerized in Table 2 for Figs. 3, 4 and 5. Thick solid curves

**Table 2** Parameters in Calculating Eqs. (3.8) and (3.9)

| Station | $\bar{U}_w$ (cm/s) | $m$ | $u_0$ (cm/s) | $u_{*w}$ (cm/s) |
|---|---|---|---|---|
| A | −23.8 | −0.8 | 3.84 | 1.30 |
| | −30.3 | −0.8 | −3.70 | 1.41 |
| B | −23.8 | −0.8 | −0.85 | 1.30 |

which are named as 'Reid' in these figures represent the results making use of Eqs. (3.8) and (3.9), but the sign is reversed. The reason that we adopt $m=-0.8$ is based on the experimental data of the Reynolds stress and will be discussed in Section 3.4. The calculated curves nearly fit to the observed data. Near the water surface and the bottom, however, they indicate slight difference. In the calculation, $u_{*w}$ was estimated so that the calculated curve show a best fit to the experimental data.

*Tsuruya et al.* (1983) obtained the velocity distribution of the drift current, assuming that the logarithmic profile can stand near the water surface and the bottom, that is

$$\bar{U}(z)=\frac{u_{*w}}{\kappa}\ln\frac{z_{0w}+a}{z_{0w}-d}-\frac{u_{*b}}{\kappa}\ln\frac{a+z_{0b}+z}{z_{0b}}. \tag{3.15}$$

From Eq. (3.15) mean velocity $\bar{U}_w$ is represented as

$$\bar{U}_w \fallingdotseq \frac{u_{*w}}{\kappa} - \frac{u_{*b}}{\kappa}\left(\ln\frac{d}{z_{0b}} - 1\right). \tag{3.16}$$

If it can be assumed that the bottom to be smooth, the logarithmic distribution of the velocity gives

$$\frac{z_{0b}u_{*b}}{\nu_w} = 0.111, \tag{3.17}$$

where $\nu_w$ is kinematic viscosity of water. The surface roughness length $z_{0w}$ can be obtained by assuming that the roughness Reynolds numbers just above and below the water surface are equal, that is

$$z_{0w} = \sqrt{\frac{\rho_w}{\rho_a}}\frac{\nu_w}{\nu_a} z_{0a}, \tag{3.18}$$

where $\nu_a$ is kinematic viscosity of air.

If $u_0$, $z_{0w}$ and $\bar{U}_w$ are known, $u_{*w}$, $u_{*b}$ and $z_{0b}$ are obtained by solving Eqs. (3.16), (3.17) and (3.18). The results are indicated as dash-dot lines in Figs. 3, 4, and 5. Although there is some difference at the center of the stream, the agreement is good near the surface and the bottom. The values of parameters employed and estimated in calculating the velocity distributions are summerized in Table 3. The estimated values of $u_{*w}$ in Table 3 are less than that in Table 2. Because both

**Table 3** Parameters in Calculating Eq. (3.15)

| Station | $\bar{U}_w$ (cm/s) | $u_0$ (cm/s) | $u_{*a}$ (cm/s) | $z_{0a}\times10^4$ (cm) | $\nu_a$ (cm²/s) | $z_{0w}\times10^4$ (cm) | $u_{*w}$ (cm/s) | $u_{*b}$ (cm/s) | $z_{0b}\times10^4$ (cm) |
|---|---|---|---|---|---|---|---|---|---|
| A | −23.8 | 3.84 | 29.18 | 2.95 | 0.158 | 5.31 | 1.17 | 1.10 | 9.89 |
| | −30.3 | −3.70 | | | | 11.1 | 1.25 | 1.35 | 8.08 |
| B | −23.8 | −0.85 | 29.04 | 5.69 | 0.156 | 5.31 | 0.992 | 1.09 | 10.7 |

estimation contain many assumptions, it is not certain for the present that which is more reasonable. In the later analysis, however, the values of $u_{*w}$ in Table 2 will be used.

The velocity distribution of the flow with adverse wind is similar to that of pipe flow. Next, we try to apply the theory obtained for the pipe flow. *Zagustin and Zagustin* (1969) studied the turbulent flow in a smooth pipe using a "balance of pulsation energy" equation. They obtained an expression for the universal law of the velocity distribution

$$\frac{U-u}{u_*} = 5.0\tanh^{-1}\left(\frac{r}{R}\right)^{\frac{3}{2}}, \tag{3.19}$$

where $U$ is the velocity at the axis of the pipe, $u$ the velocity at a given point in the pipe, $u_*$ the friction velocity, $r$ the radial distance measured from the axis of the pipe and $R$ the radius of the pipe. If we regard the flow in this experiment with the wind shear behaving similar with a pipe flow, the relation (3.19) can be used by separating the flow field into two regions at the height where the velocity gradient diminishes. This condition is satisfied when $-z/d=0.555$. The calculated

distribution using the *Zagustin and Zagustin's* theory is represented in Fig. 3. For the upper layer, the theoretical value is small compared with the experimental data.

### 3.4 Reynolds Stress

Turbulent motion may be defined as a randomly fluctuating motion superimposed on a mean motion. Instantaneous velocity is then given by

$$U=\overline{U}+u, \qquad W=\overline{W}+w, \tag{3.20}$$

where $\overline{U}$ and $\overline{W}$ $(=0)$ are the mean velocities and $u$ and $w$ represent the turbulent motions in $x$ and $z$ direction, respectively.

The Reynolds stress $\tau$ and the intensities of the turbulent motions can be written as

$$\tau=-\rho_w\overline{uw}, \quad u'^2=\overline{u^2}, \quad w'^2=\overline{w^2}, \tag{3.21}$$

where $u'$ and $w'$ are the root-mean-square turbulence-velocity components in the $x$ and $z$ direction, respectively. From the first equation of (3.21), the shear velocity $u_*$ can be written as $u_*^2=-\overline{uw}$.

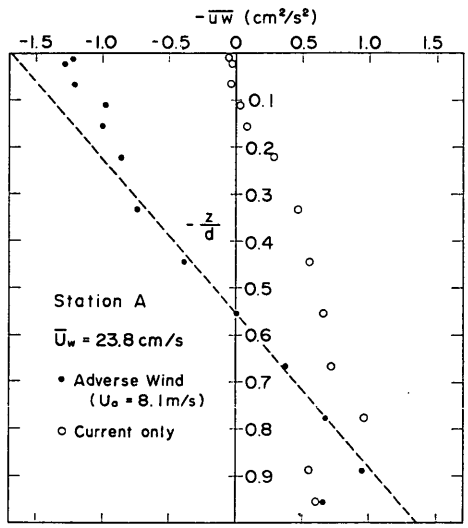


**Fig. 6** Reynolds Stress (Station A, $\overline{U}_w=23.8$ cm/s)

Figure 6 shows the distribution of the measured Reynolds stress for both adverse wind and current only cases at the station A. In the case of adverse wind, the Reynolds stress lie close to the linear distribution except near the water surface and the bottom. The height at which the Reynolds stress becomes zero is $-z/d=0.555$. The distributions of the Reynolds stress in other cases are represented in Figs. A-1 and A-2. Figure 7 summarizes the Reynolds stress normalized by a surface shear velocity. In the middle part of the flow three cases lie close to the

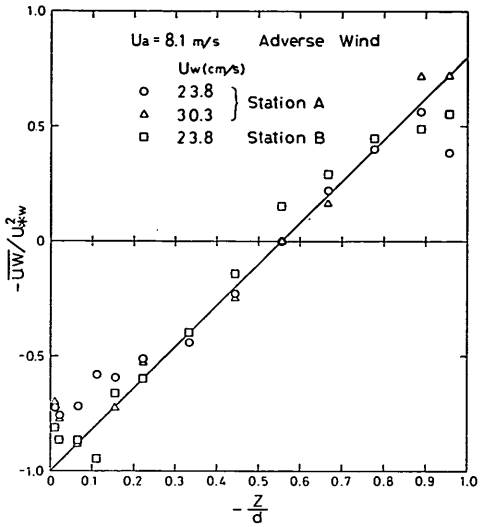


**Fig. 7** Reynolds Stress Normalized by Surface Shear Velocity

one linear distribution. If we assume that the Reynolds stress follow a linear distribution, it can be considered from the figure that the bottom shear stress is 80% of the surface shear stress. This is why that we adopt $m=-0.8$ in the calculation of *Reid's* distribution in Section 3.3.

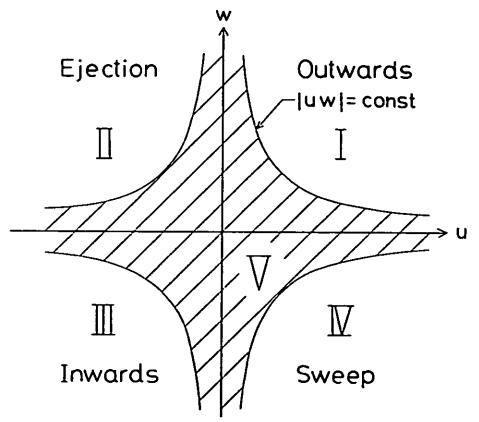


**Fig. 8** Sketch of 'Hole' Region in the $u$, $w$ Plane

The conditional sampling technique as described below is used in order to investigate the detailed characteristics of the Reynolds stress. The $u$-$w$ plane is devided into five regions as shown in Fig. 8. In this figure, the hatched region is called as a 'hole', and is bounded by the curves $|uw|=$const. A parameter $H'$ is introduced so as to $|uw|=H'u'w'$. The parameter $H'$ is called the hole size after *Lu*

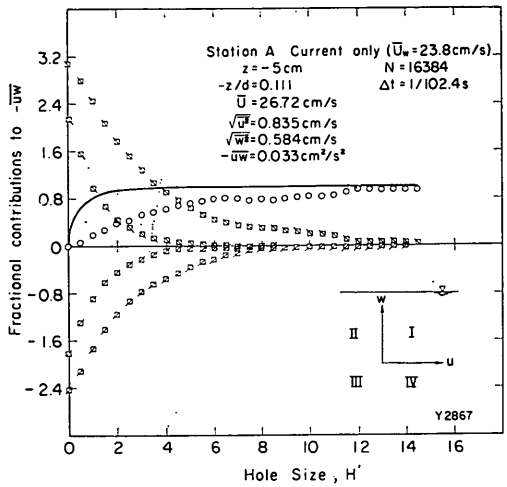


**Fig. 9** Contributions to $-\overline{uw}$ from Different Events (Station A, Current Only, $\bar{U}_w$=23.8 cm/s, $z$=−5 cm). $S_{1,H'}$: ⊿, $S_{2,H'}$: ▽, $S_{3,H'}$: ⊿, $S_{4,H'}$: ▽, Contribution from 'hole': ○, Fraction of Time in 'hole': —.

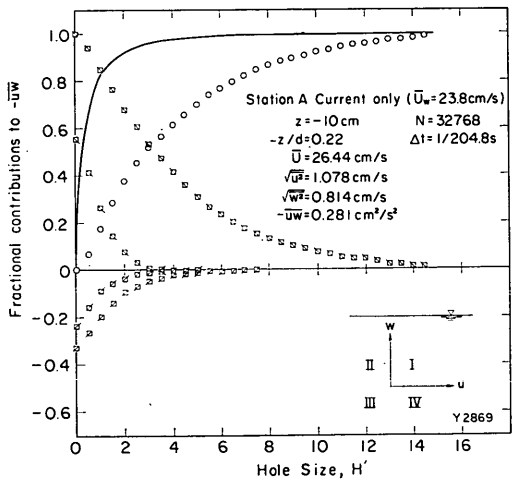


**Fig. 10** Contributions to $-\overline{uw}$ from Different Events (Station A, Current only, $\bar{U}_w$=23.8 cm/s, $z$=−10 cm). Notation as in **Fig. 9**

*and Willmarth* (1973).

The contributions to $\overline{uw}$ from the four quadrants are computed from the following equations:

$$\langle uw\rangle_{i,H'}=\lim_{T\to\infty}\frac{1}{T}\int_0^T u(t)w(t)D_{i,H'}[u(t),\ w(t)]dt,\quad (i=1,2,3,4),\quad (3.22)$$

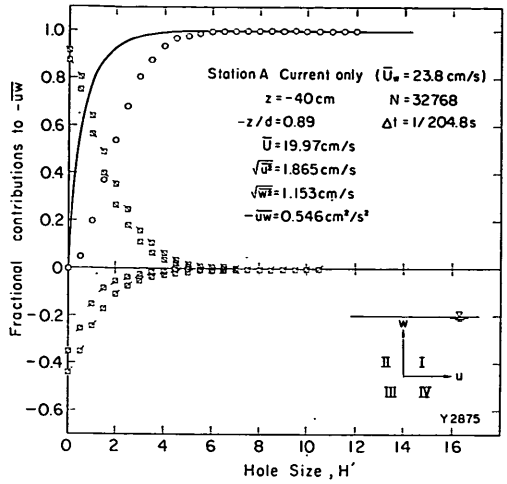


**Fig. 11** Contributions to $-\overline{uw}$ from Different Events (Station A, Current Only, $\bar{U}_w$=23.8 cm/s, $z$ =−40 cm). Notation as in **Fig. 9.**

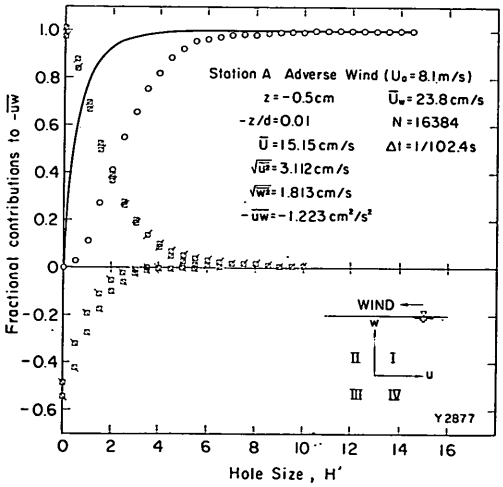


**Fig. 12** Contributions to $-\overline{uw}$ from Different Events (Station A, Adverse Wind, $\bar{U}_w$=23.8 cm/s, $z$=−0.5 cm), Notation as in **Fig. 9.**

where $<>$ represents the conditional sampling and

$$D_{i,H'}(u,w)=\begin{cases}1, & \text{if } |uw|>H'u'w' \text{ and the point}(u,w) \text{ in the i-th quadrant,}\\ 0, & \text{otherwise.}\end{cases} \tag{3.23}$$

The contribution rate from the each quadrant to the Reynolds stress is therefore

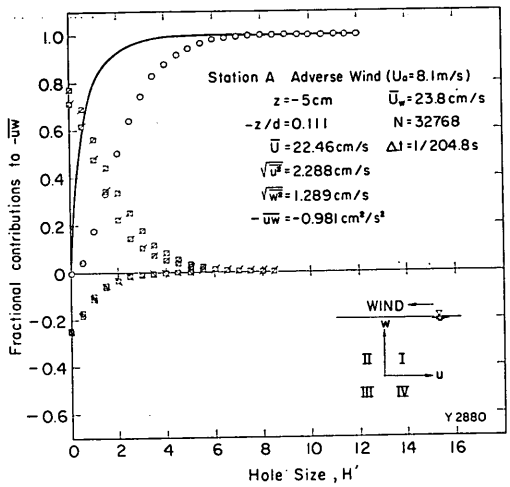


**Fig. 13** Contributions to $-\overline{uw}$ from Different Events (Station A, Adverse Wind, $\bar{U}_w$=23.8 cm/s, $z$=−5 cm). Notation as in **Fig. 9.**

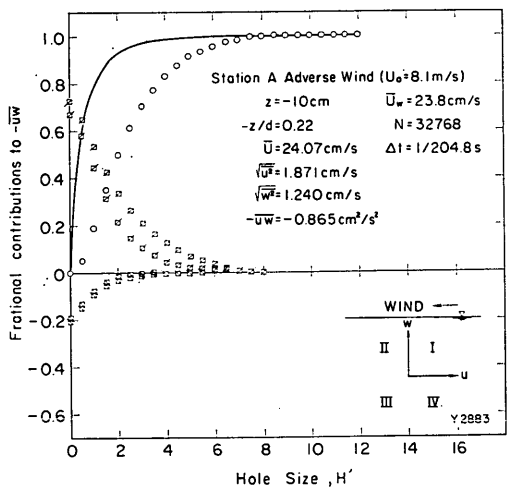


**Fig. 14** Contributions to $-\overline{uw}$ from Different Events (Station A, Adverse Wind, $\bar{U}_w$=23.8 cm/s, $z$=−10 cm). Notation as in **Fig. 9.**

$$S_{t,H'}=\langle uw\rangle_{t,H'}/\overline{uw}. \tag{3.24}$$

The contribution to $\overline{uw}$ from the 'hole' region is obtained from

$$S_{5,H'}=\frac{1}{\overline{uw}}\lim_{T\to\infty}\frac{1}{T}\int_0^T u(t)w(t)D_{5,H'}[u(t),w(t)]dt, \tag{3.25}$$

where

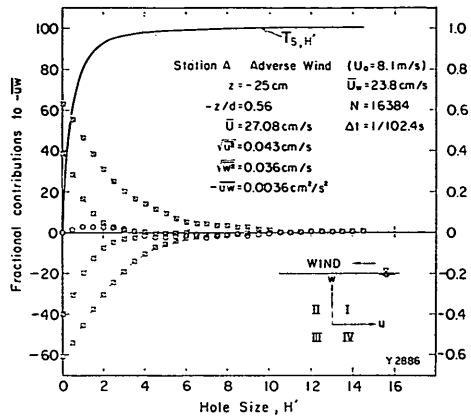


**Fig. 15** Contributions to $-\overline{uw}$ from Different Events (Station A, Adverse Wind, $\overline{U}_w=23.8$ cm/s, $z=-25$ cm), Notation as in **Fig. 9.**

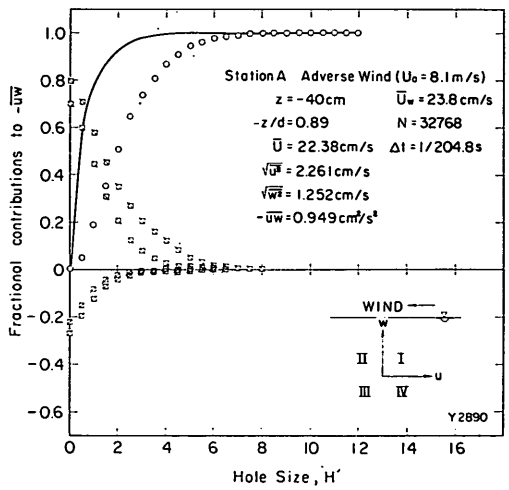


**Fig. 16** Contributions to $-\overline{uw}$ from Different Events (Station A, Adverse Wind, $\overline{U}_w=23.8$ cm/s, $z=-40$ cm), Notation as in **Fig. 9.**

$$D_{5,H'}(u,w)=\begin{cases}1, & \text{if } |uw|\leqq H'u'w',\\ 0, & \text{otherwise.}\end{cases} \tag{3.26}$$

These five contributions are all functions of the hole size and must satisfy the following relation

$$\sum_{i=1}^{4} S_{i,H'}+S_{5,H'}=1. \tag{3.27}$$

The time fraction during which each contribution is being made is

$$T_{i,H'}=\lim_{T\to\infty}\frac{1}{T}\int_0^T D_{i,H'}[u(t),w(t)]dt,\quad (i=1,2,3,4,5), \tag{3.28}$$

where $D_{i,H'}$ is represented by Eqs. (3.23) and (3.26). It is customary to label the events defined by the four quadrants $i$ as outward interactions ($i=1$; $u>0$, $w>0$), ejections ($i=2$; $u<0$, $w>0$), inward interactions ($i=3$; $u<0$; $w<0$) and sweeps ($i=4$; $u>0$, $w<0$), respectively.

Figures 9~11 represent the fractional contributions from different events at various elevations for the case of current only. The directions of the line segments of open squares in the figures represent the quadrants to which squares belong as illustrated in the caption of Fig. 9. In these figures, contributions from the second (ejection) and the fourth (sweep) quadrants are remarkable as usually seen in the boundary layer flow. When wind acts on the water surface, on the contrary, contributions from the first and the third quadrants dominate (see Figs. 12~16). It can be deduced from the figures that the water surface which suffers the wind shear resembles like a wall. In this case, the contributions from the third and the first quadrants can be considered as ejections and sweeps, respectively. Near the water surface, the contributions from the third quadrant is slightly greater than that from the first quadrant. The contributions in Fig. 15 was measured at $z=-25$ cm and the Reynolds stress was nearly zero as can be confirmed from Fig. 6. It is noticeable that when the Reynolds stress is nearly zero, contributions from the second and the third quadrants are balanced. Moreover, contributions from the first and the fourth quadrants are also balanced.

### 3.5 Turbulence Intensities and Spectra

When detergent is applied, the water properties are slightly varied. For example, surface tension decreases to a value of 70% of tap water and wind waves cannot develop under the action of wind even at relatively high wind speed. Eddy viscosity was also measured but significant difference could not be recognized. As it is suspected that detergent influence the turbulent structures, turbulent spectra are investigated in a detergent added water. In the same manner as the mean current distribution, frequency spectra of turbulent fluctuations in the cases with and without detergent are compared. Figure 17 shows the frequency spectra of $u$ component and Fig. 18 shows that of $w$ component. In the figures both cases yield the same spectra. This means that the influence of the detergent can be ignored in turbulent streams. In the following discussions, therefore, we consider that the detergent have nothing to do with the turbulence intensities and spectra. In this section we investigate an universal relation of turbulent intensities under the action of wind and the characteristics of the spectrum of turbulence.

In Figs. 19 and 20, relative turbulence intensities $u'/\bar{U}$ and $w'/\bar{U}$ are represented. In the figures the data of *McQuivey and Richardson* (1969) are also plotted. It is evident that in the case of current only, distributions of both $u$ and $w$ components resemble like the data of *McQuivey and Richardson*. Near the water surface, however, the difference for the $u$ components becomes noticeable. As experiments by *McQuivey and Richardson* were conducted in an open channel with 3 cm water depth, it can be considered that the difference between our data and that of *McQuivey and Richardson's* is originated from the variation of the influence of surface fluctuations which is called as "inactive component" (*Bradshaw*, 1967A). In the present experiment, water depth was 45 cm and no significant surface fluctua-

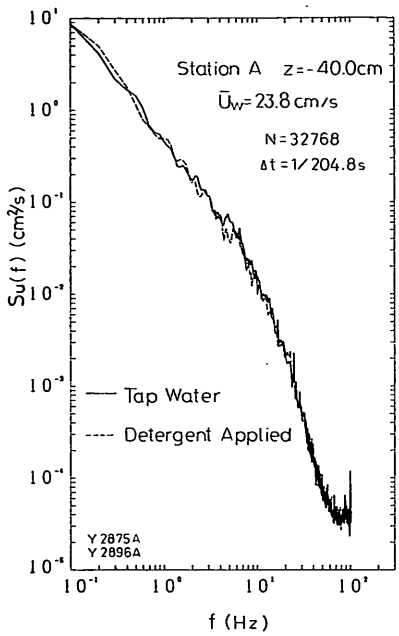


**Fig. 17** Longitudinal Turbulence Spectra (Tap Water and Detergent Applied)

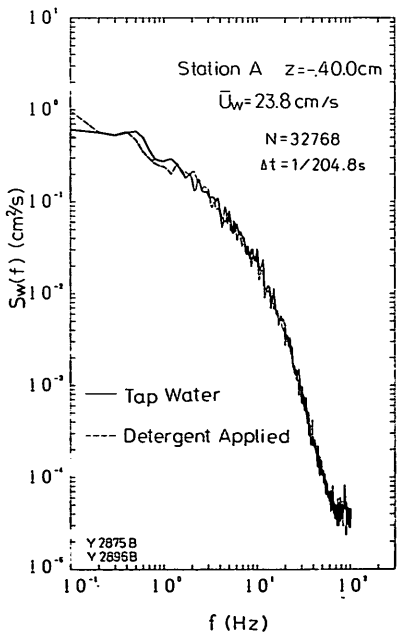


**Fig. 18** Vertical Turbulence Spectra (Tap Water and Detergent Applied)

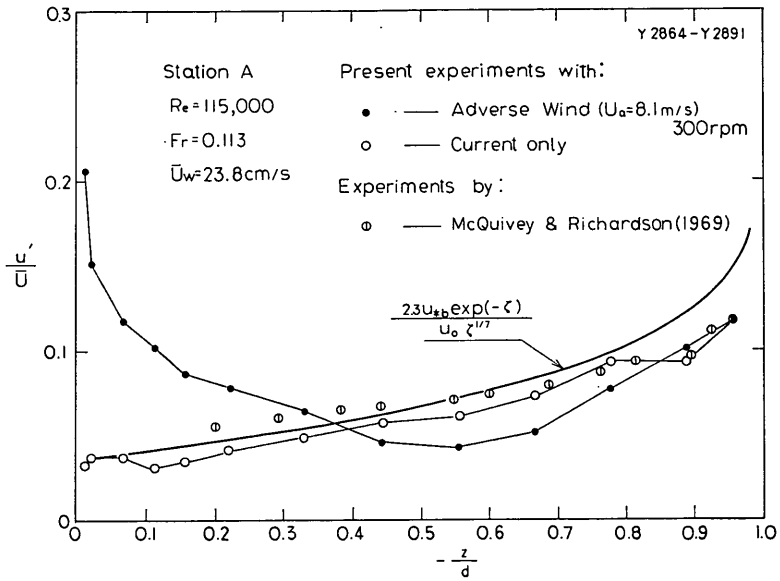


**Fig. 19** Longitudinal Turbulence Intensities (Station A, $\bar{U}_w = 23.8$ cm/s)

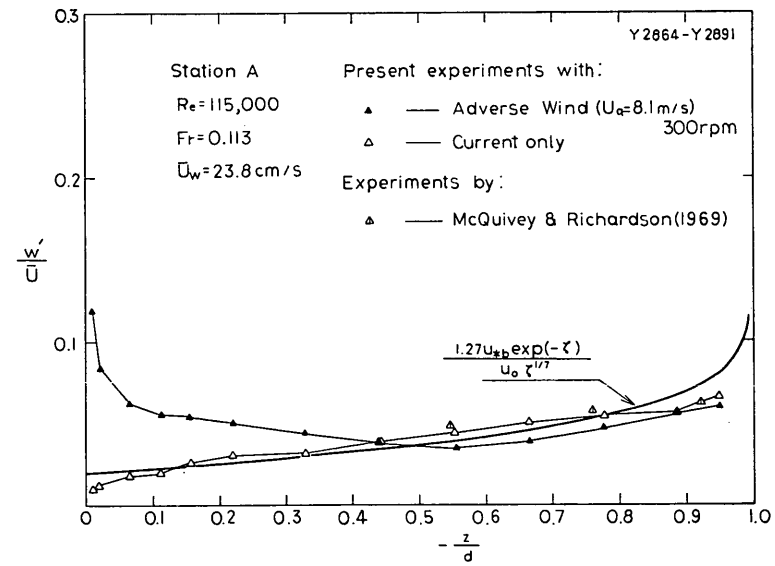


**Fig. 20** Vertical Turbulence Intensities (Station A, $\bar{U}_w = 23.8$ cm/s)

tions could be observed.

*Nezu* (1977) has studied the turbulence intensities in an open channel flow and found the universal distributions of turbulence intensities non-dimensionalized by the shear velocity $u_{*b}$ at the bed.

They are represented as

$$u'/u_{*b}=D_1\exp(-\lambda\zeta/2),\quad D_1=2.30,$$
$$w'/u_{*b}=D_2\exp(-\lambda\zeta/2),\quad D_2=1.27 \tag{3.29}$$

where $u'$ and $w'$ are the root-mean-square turbulence-velocity components, $\lambda$ the constant and is taken to be 2.0 after *Nezu* and $\zeta=(d+z)/d$.

Now we use the 1/7-th power law as a mean velocity distribution. With the aid of Eq. (3.29), the relative turbulence intensities can be written as

$$\frac{u'}{\overline{U}}=\frac{2.3\,u_{*b}\exp(-\zeta)}{u_0\zeta^{1/7}},$$
$$\frac{w'}{\overline{U}}=\frac{1.27\,u_{*b}\exp(-\zeta)}{u_0\zeta^{1/7}}. \tag{3.30}$$

Equation (3.30) are represented in Figs. 19 and 20 as solid curves. Except near the bottom where $-z/d=1.0$, the agreement between the *Nezu's* universal functions (3.29) and our experimental data are fairly good.

When adverse wind acts on the surface of the stream, turbulence intensities near the water surface increase compared with the case of current only. On the other hand, they decrease where the relative depth $-z/d$ is lower than 0.4. As will be discussed later, turbulence production by the Reynolds stress can be represented as

$$-\rho_w\,\overline{uw}\frac{d\overline{U}}{dz}. \tag{3.31}$$

From Fig. 6 it is seen that the Reynolds stress at the elevation $-z/d=0.55$ is zero. As a result, turbulence intensities produced by the Reynolds stress would be very small as confirmed in Fig. 19.

When wind blows on the water surface the development of turbulence intensities from the surface can be considered to have the same form as that from the bottom as represented in Eq. (3.29). Consequently, the turbulence intensities can be

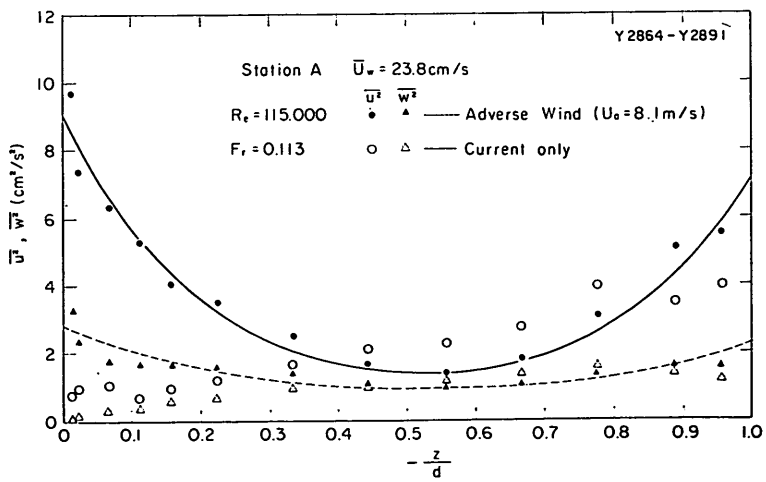


**Fig. 21** Mean Square Values of Velocity Fluctuations (Station A, $\overline{U}_w$=23.8 cm/s)

written as

$$u'^2 = G_{1b}^2 u_{*b}^2 \exp(-\lambda_1 \zeta) + G_{1w}^2 u_{*w}^2 \exp\{\lambda_1'(\zeta-1)\},$$
$$w'^2 = G_{2b}^2 u_{*b}^2 \exp(-\lambda_2 \zeta) + G_{2w}^2 u_{*w}^2 \exp\{\lambda_2'(\zeta-1)\}. \quad (3.32)$$

It was assumed that the turbulence intensities from the water surface and the bottom can be added linearly. Moreover we assume that the constants are the same as *Nezu's* constants $D_1$ and $D_2$, namely, $G_{1b}=G_{1w}=2.3$, $G_{2b}=G_{2w}=1.27$. Furthermore, assuming $\lambda_1=\lambda_1'$ and $\lambda_2=\lambda_2'$ and making use of the experiental data, $\lambda_1$ and $\lambda_2$ can be obtained as

$$\lambda_1=4.86,$$
$$\lambda_2=3.37. \quad (3.33)$$

In Fig. 21 calculated curves (3.32) are shown as solid and broken lines for $u$ and $w$ components, respectively. The agreement is fairly good. In the calculation $u_{*b}=1.15$ cm/s and $u_{*w}=1.3$ cm/s were used. The relative turbulent intensities and the mean square values for another cases are shown in Figs. A-3~A-6.

The one-dimensional power-spectral density function was computed using the FFT algorithm. Figures 22 and 23 show an example of the frequency spectra of the cases with and without wind. Figure 22 shows the power spectra of $u$ and $w$ components for the case without wind and Fig. 23 shows that of the case with wind ($U_a=8.1$ m/s). It can be considered that the sharp peak in Fig. 23 is caused by the wind vibration of the pipe attatched to the traverse system to which v-probe was furnished.

For the isotropic turbulence, one-dimensional spectra of $u$ and $w$ components have the following relation

$$S_w(k)=\frac{1}{2}\left[S_u(k)-k\frac{\partial S_u(k)}{\partial k}\right], \quad (3.34)$$

where $k=2\pi f/\overline{U}$ is a wave number (*Hinze*, 1975, p. 204). In the inertial subrange $S_u(k)$ has the slope of $-5/3$ and Eq. (3.34) reduces to

$$S_w(k)=\frac{4}{3}S_u(k). \quad (3.35)$$

In Figs. 22 and 23 we admit that in the inertial subrange the relation (3.35) can hold approximately. All the frequency spectra of $u$ component are converted into wave number spectra and some of them are shown in Figs. 24~35. They correspond to the case S-1. Near the water surface, spectral components in the case of adverse wind are exceedingly greater than that in the case of current only. On the contrary, in the middle part of the flow ($-25>z>-35$ cm), spectral components in the case of current only are slightly greater than that in the case of adverse wind. This corresponds to the situation of turbulence intensities we have already shown in Figs. 19 and 21. Near the bottom, turbulent spectra are not so affected by the wind.

According to the previous studies in open channel flow, the spectrum of turbulence has an universal form (e.g., *Nezu*, 1977). For simplicity, we consider the one-dimensional energy spectrum $S(k)$ in the wave number field $k$, where $k=2\pi f/\overline{U}$, $f$

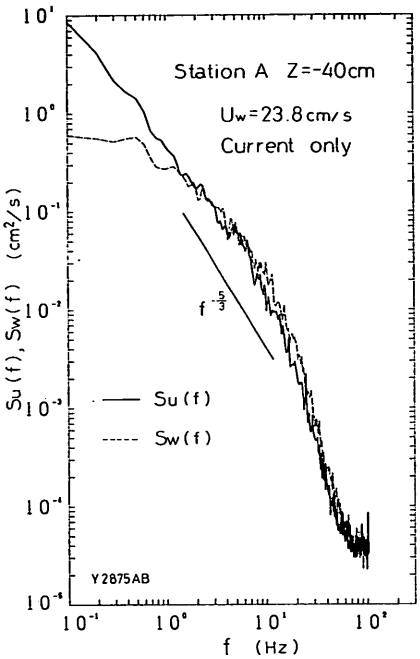


**Fig. 22** Turbulence Spectra (Station A, Current only, $\bar{U}_w = 23.8$ cm/s)

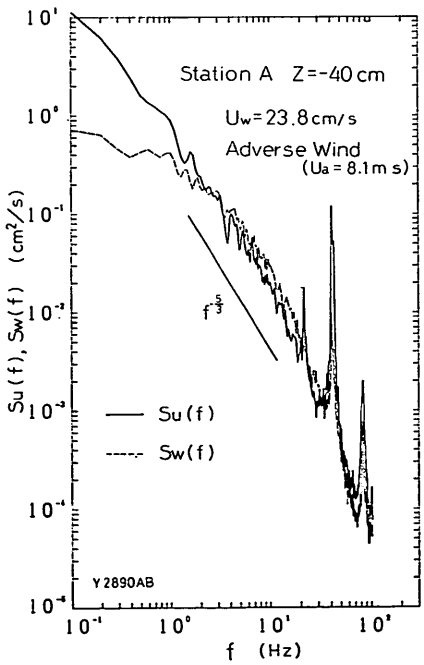


**Fig. 23** Turbulence Spectra (Station A, Adverse Wind, $z = -40$ cm, $\bar{U}_w = 23.8$ cm/s)

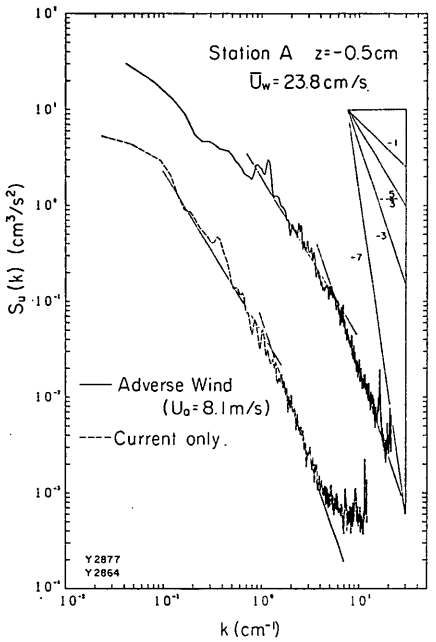


**Fig. 24** Longitudinal Wave Number Spectra with Current Only and Adverse Wind (Station A, $z=-0.5$ cm, $\bar{U}_w=23.8$ cm/s)

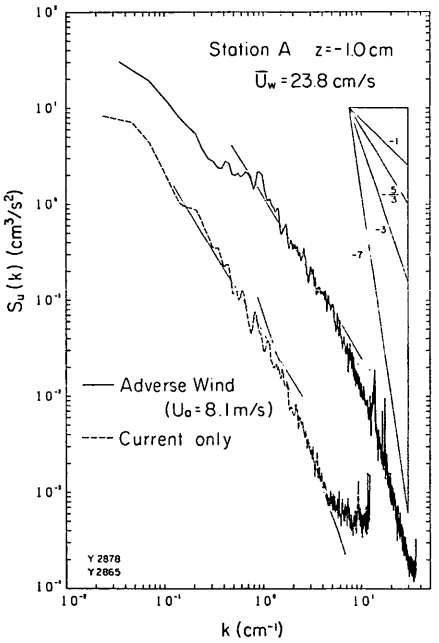


**Fig. 25** Longitudinal Wave Number Spectra with Current only and Adverse Wind (Station A, $z=-1$ cm, $\bar{U}_w=23.8$ cm/s)

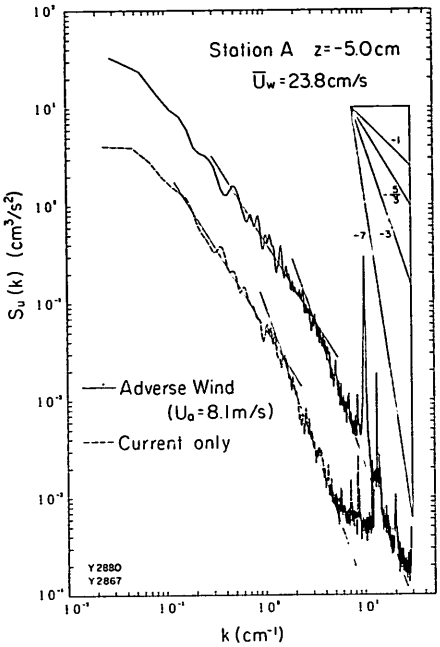


**Fig. 26** Longitudinal Wave Number Spectra with Current Only and Adverse Wind (Station A, $z=-5$ cm, $\bar{U}_w=23.8$ cm/s)

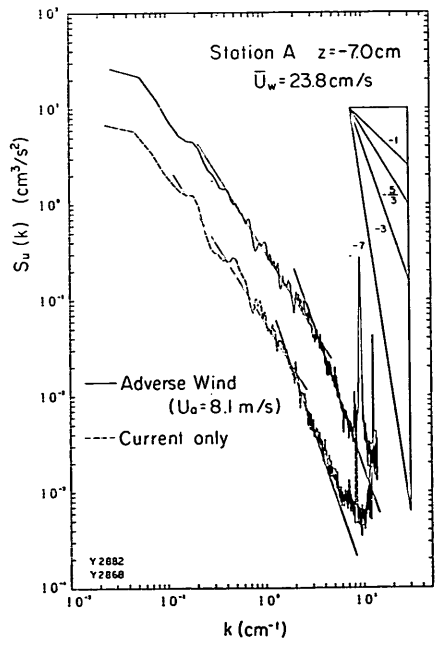


**Fig. 27** Longitudinal Wave Number Spectra with Current Only and Adverse Wind (Station A, $z=-7$ cm, $\bar{U}_w=23.8$ cm/s)

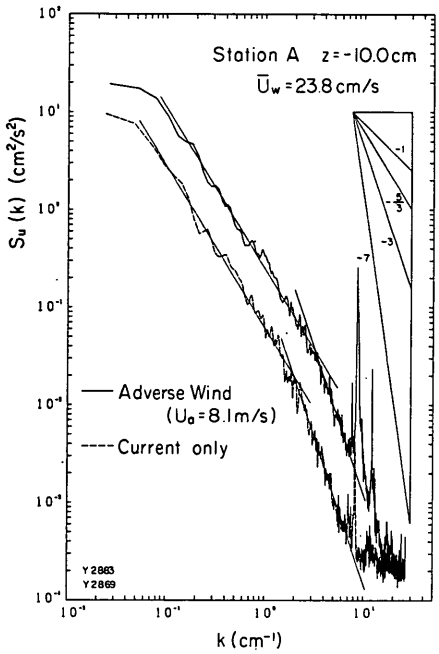


**Fig. 28** Longitudinal Wave Number Spectra with Current Only and Adverse Wind (Station A, $z=-10$ cm, $\bar{U}_w=23.8$ cm/s)

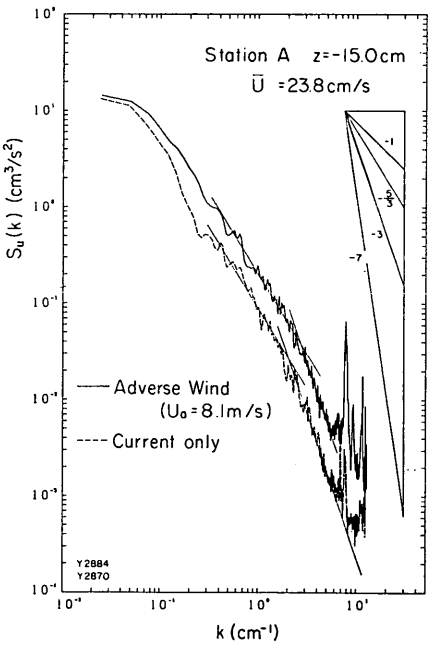


**Fig. 29** Longitudinal Wave Number Spectra with Current Only and Adverse Wind (Station A, $z=-15$ cm, $\bar{U}_w=23.8$ cm/s)

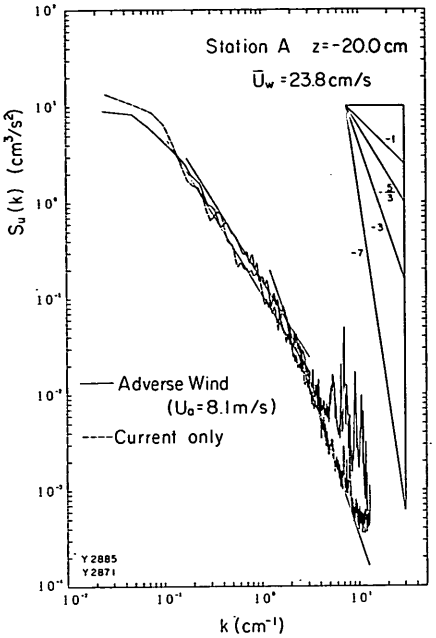


**Fig. 30** Longitudinal Wave Number Spectra with Current Only and Adverse Wind (Station A, $z=-20$ cm, $\bar{U}_w=-23.8$ cm/s)

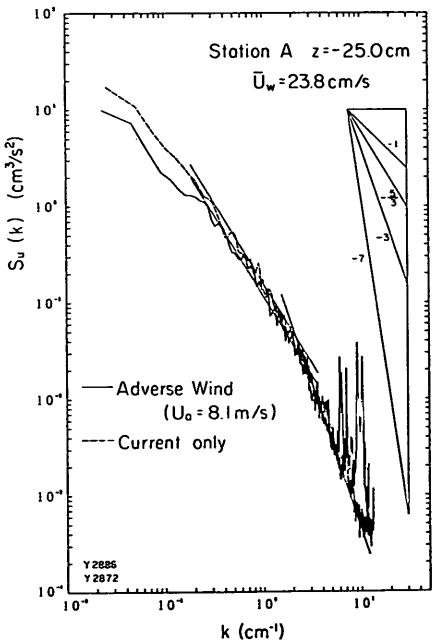


**Fig. 31** Longitudinal Wave Number Spectra with Current Only and Adverse Wind (Station A, $z=-25$ cm, $\bar{U}_w=23.8$ cm/s)

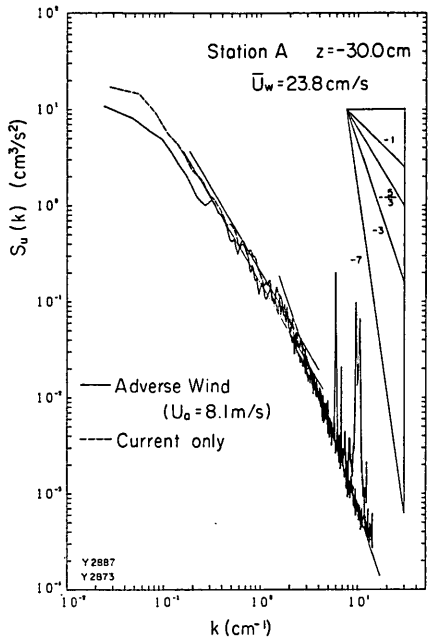


**Fig. 32** Longitudinal Wave Number Spectra with Current Only and Adverse Wind (Station A, $z=-30$ cm, $\bar{U}_w=-23.8$ cm/s)

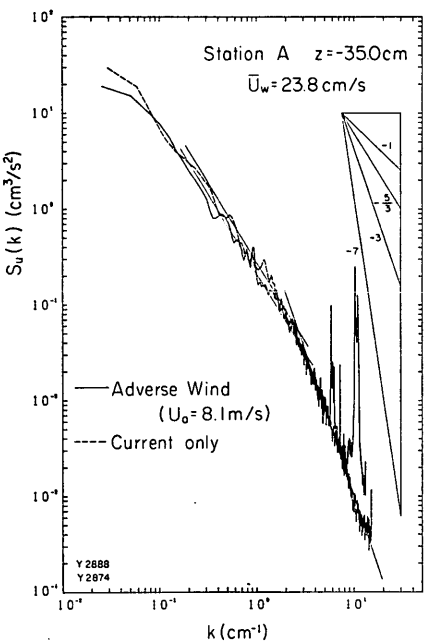


**Fig. 33** Longitudinal Wave Number Spectra with Current Only and Adverse Wind (Station A, $z=-35$ cm. $\bar{U}_w=23.8$ cm/s)

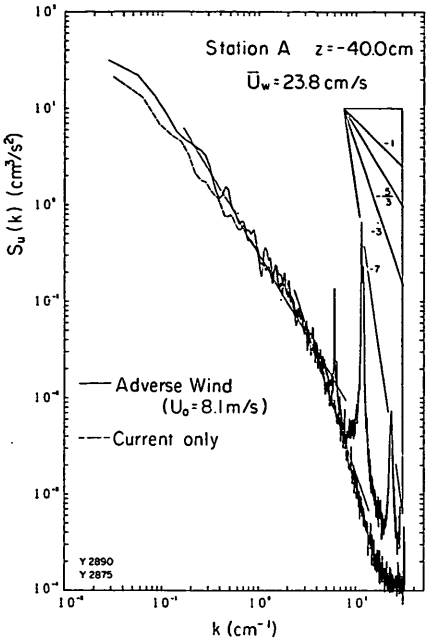


**Fig. 34** Longitudinal Wave Number Spectra with Current only and Adverse Wind (Station A, $z=-40$ cm, $\bar{U}_w=23.8$ cm/s)

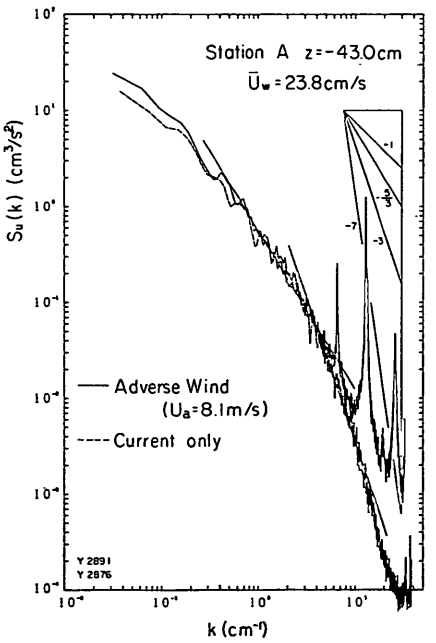


**Fig. 35** Longitudinal Wave Number Spectra with Current Only and Adverse Wind (Station A, $z=-43$cm, $\bar{U}_w=23.8$cm/s)

and $\overline{U}$ are frequency and mean current velocity, respectively. For the large Reynolds numbers the form of $S(k)$ in the inertial subrange can be expressed as

$$S(k)=A\varepsilon^{\frac{2}{3}}k^{-\frac{5}{3}}, \tag{3.36}$$

where $\varepsilon$ is the dissipation rate by turbulence per unit mass and $A$ is an absolute constant.

In the viscous dissipation range, *Inoue* (1952) have obtained the relation as follows

$$S(k)\sim\varepsilon\nu^{-1}k^{-3}, \tag{3.37}$$

where $\nu$ is kinematic viscosity of the fluid. *Heisenberg* (see for example, *Hinze*, 1975, p. 245), on the other hand, have obtained another relation as follows

$$S(k)=\frac{2}{63}\cdot\left(\frac{\alpha}{2}\right)^2\cdot\left(\varepsilon\nu^5\right)^{\frac{1}{4}}\cdot\left(\frac{k}{k_d}\right)^{-7}, \tag{3.38}$$

where $\alpha$ is the constant of proportionality, $k_d=1/\eta$ and $\eta=(\nu^3/\varepsilon)^{1/4}$ is the Kolmogoroff length scale. In Figs. 24~35 spectral shapes are remarkably similar and each spectra has the $-5/3$ law for the inertial subrange and the $-3$ law for the viscous dissipation range.

The coordinates are non-dimensionalized using $S_0=(\varepsilon\,\nu_w^5)^{1/4}$ and the Kolmogoroff length scale $\eta$, where $\nu_w$ is kinematic viscosity of water. Figures 36 and 37 show an example of the normalized wave number spectra. All the spectral profiles collaps to a single curve except at the low wave numbers observed near the water surface

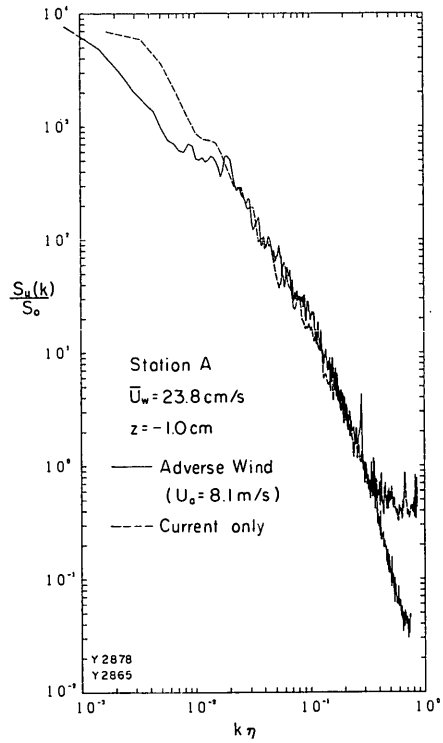


**Fig. 36** Normalized Energy Spectra ($z=-1$cm)

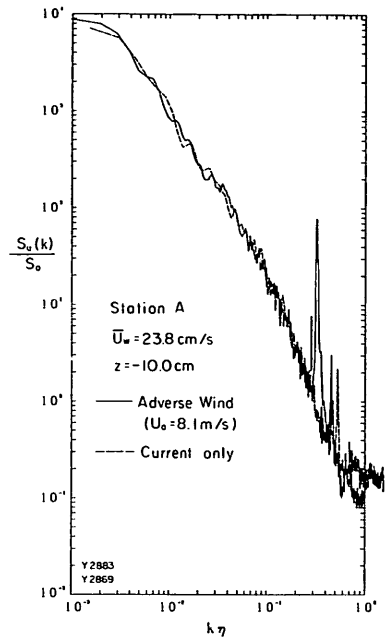


**Fig. 37** Normalized Energy Spectra ($z=-10$cm)

(e.g., $z=-1$ cm). This indicates that in the case of the adverse wind, the relation (3.36) and (3.37) can hold the same as in the case of usual open channel flow.

The dissipation may be calculated directly from the measured spectral-energy function (*Panofsky and Dutton*, 1983, p. 333)

$$\varepsilon=15\,\nu_w\int_0^\infty k^2 S_u(k)dk, \tag{3.39}$$

where $k^2S_u(k)$ is usually called a "dissipation spectrum". The dissipation spectrun is illustrated in Fig. 38 in the case S-1 and the elevation $z=-1.0$ cm in the logarithmic coordinates and in Fig. 39 in the case S-2 ($z=-1.0$ cm) in the normal coordinates. In calculating $\varepsilon$ using Eq. (3.39) from the observed spectrum, it is difficult to determine the limit of integration. If the wave number spectrum has the $-3$ law and does not have the $-7$ law in high wave number region, the dissipation spectrum does not decrease rapidly as the wave number increases and the integral value in Eq. (3.39) changes according to the limit of integration.

There is an another way to evaluate the viscous dissipation rate $\varepsilon$, which uses the spectral function (3.36). If the universal constant $A$ is previously known, we can evaluate $\varepsilon$ making an application Eq. (3.36) to the inertial subrange of the calculated wave number spectrum. Based on the many experimental investigations, *Bradshaw* (1967B) concluded that the constant is

$$A=0.5\pm0.05, \tag{3.40}$$

in the range of $R_{e\lambda}=\sqrt{\overline{u^2}}\,\lambda_E/\nu=100\sim10000$,
where $\lambda_E$ is the Taylor's microscale. In this study, $A=0.47$ is adopted (*Grant et al.*, 1962), (*Imamoto*, 1977). In order to compare the two methods, $\varepsilon$ is calculated by

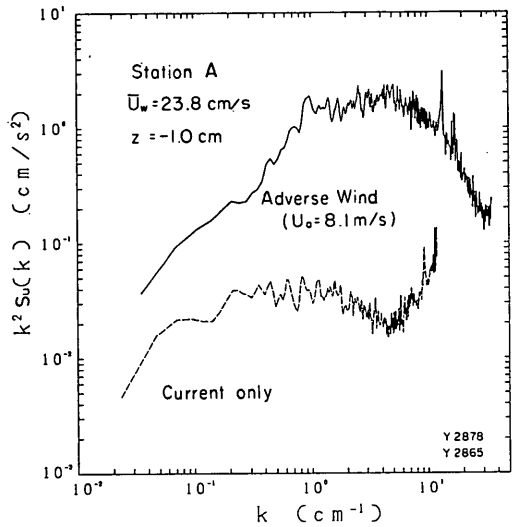


**Fig. 38** Dissipation Spectra (Station A, $z=-1$cm, $\bar{U}_w=23.8$ cm/s)

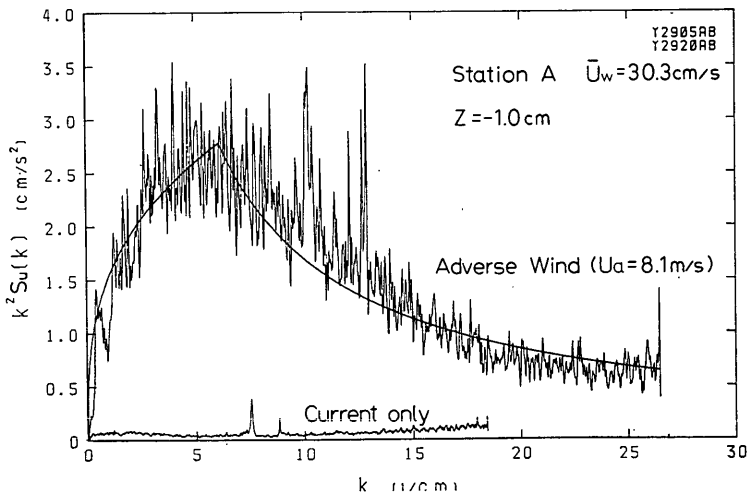


**Fig. 39** Dissipation Spectra (Station A, $z=-1$cm, $\bar{U}_w=30.3$ cm/s)

both methods. In the case of Fig. 39, spectrum function in the inertial subrange and viscous dissipation range for the case of adverse wind are

$$\begin{aligned} S_u(k) &= 1.52\,k^{-\frac{5}{3}}, \quad 0<k<6.12, \\ &= 17.0\,k^{-3}, \quad 6.12 \leqq k < k_*. \end{aligned} \tag{3.41}$$

The dissipation spectrum using Eq. (3.41) is represented in Fig. 39 as a solid curve which intersects at $k=6.12$. The substitution Eq. (3.38) in Eq. (3.39) leads to

$$15\nu_w\int_0^{k_*} k^2 S_u(k)dk = 15\nu_w(17\ln k_* - 18.0), \tag{3.42}$$

where $k_*$ is the upper limit of the integral and $\nu_w=0.00877$. On the other hand, applying Eq. (3.36) to the observed spectrum we can get

$$\varepsilon = 5.82. \tag{3.43}$$

Equating Eq. (3.42) and Eq. (3.43) yields

$$k_* = 38.9. \tag{3.44}$$

This exceeds the observed range. Because of the difficulties stated above and the scatter of the dissipation spectrum as recognized from Fig. 39, the relation (3.39) was not used in calculating the dissipation.

For two-dimensional flow, the turbulent kinetic-energy equation reduces to

$$\overline{\rho uw}\frac{d\bar{U}}{dz} = \frac{d}{dz}\overline{[\rho w(u^2+v^2+w^2)+wp]} + \mu_w\overline{\left(\frac{u_i}{x_j}\right)\left(\frac{u_i}{x_j}\right)}, \tag{3.45}$$

where $v^2$ is the turbulence intensity in $y$ direction perpendicular to $x$-$z$ plane and $p$ the pressure (*McQuivey and Richardson*, 1969). The left hand side of Eq. (3.45) represents the production by the Reynolds stress. The first term on the right hand side is the energy diffusion by turbulence, and the last term is the dissipation $\varepsilon$ by the breakdown of large eddies into small ones. The distributions of each term in

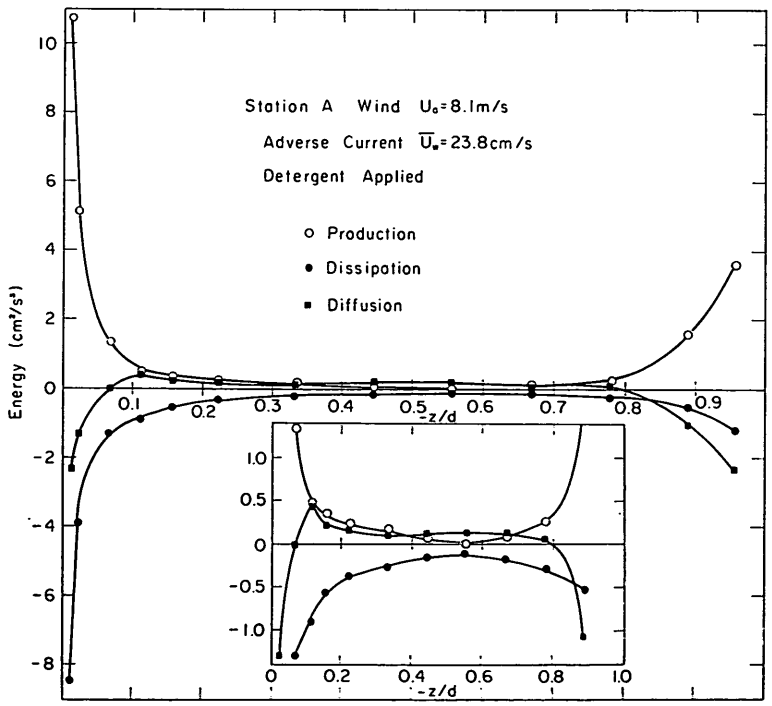


**Fig. 40** Distribution of Terms Appearing in the Mean Energy Equation

Eq. (3.45) are shown in Fig. 40. As the diffusion term could not be measured directly, it was calculated by making use of Eq. (3.45). Near the water surface, production and dissipation term become great. This can be deduced from Fig. 3, because velocity gradient near the surface becomes very large when adverse wind blows on the surface.

### 3.6 Diffusion Coefficient

In the case that the turbulence is homogeneous and stationary, i.e. if the average properties are uniform in space and steady in time, *Taylor* (1921) obtained the expression for the mean square $\overline{Z^2}$ of a large number of samples

$$\frac{d\overline{Z^2}}{dt}=2\overline{w_L^2}\int_0^t {}_wR_L(\tau)d\tau, \tag{3.46}$$

and

$$\overline{Z^2}(T)=2\overline{w_L^2}\int_0^T\int_0^t {}_wR_L(\tau)d\tau dt, \tag{3.47}$$

where $Z$ is the distance traversed by a particle in time $T$, $w_L^2$ the Lagrangian mean-square turbulence-velocity component in $z$ direction and ${}_wR_L(\tau)$ is the Lagrangian autocorrelation coefficient. The subscript $w$ represents that the autocorrelation coefficient is calculated for $w$ components. Integration of Eq. (3.47) by parts gives

$$\overline{Z^2}(T)=2\overline{w_L^2}\int_0^T(T-\tau){}_wR_L(\tau)d\tau. \tag{3.48}$$

The coefficient ${}_wR_L(\tau)$ should be unity when $\tau=0$ and is effectively zero for large $\tau$, say $\tau>t_1$. Hence, for small $T$

$$\overline{Z^2}(T)=\overline{w_L^2}T^2, \tag{3.49}$$

and for large $T$

$$\overline{Z^2}(T)=2T_L\overline{w_L^2}T, \tag{3.50}$$

where $T_L$ is a constant time-scale of turbulence and defined by

$$T_L=\int_0^\infty {}_wR_L(\tau)d\tau.$$

The flux $F$ of the property across a fixed surface due to the turbulent motion is effectively defined by the following relation

$$F=-K(T)\frac{\partial C}{\partial z}, \tag{3.51}$$

where $K(T)$ is the diffusion coefficient and $\partial C/\partial z$ is the gradient, normal to the surface, of the concentration of the property undergoing diffusion.

The diffusion coefficient $K(T)$ has the dimension of [length × velocity] and can be represented as the average of the multiplication of the velocities and displacements of fluid particles which transport any diffusible property. Thus, the diffusion coefficient is expressed as

$$K(T)=\overline{w_L Z}=\overline{Z\frac{dZ}{dT}}=\frac{1}{2}\frac{d\overline{Z^2}}{dT}. \tag{3.52}$$

From Eqs. (3.46) and (3.52) the diffusion coefficient can be written as

$$K(T)=\overline{w_L^2}\int_0^{t_1} {}_wR_L(\tau)d\tau, \tag{3.53}$$

where $t_1$ is the value of $\tau$ beyond which ${}_wR_L(\tau)$ remains zero. On the basis of observations in the atmosphere, *Hay and Pasquill* (1957) concluded that the Lagrangian correlation fell off much more slowly than did the autocorrelation of the velocity component measured at a fixed point, and in their later study (1959) they adopted a simple hypothesis of the following:

$${}_wR_L(\xi)={}_wR_E(t), \qquad \text{when} \quad \xi=\beta t, \tag{3.54}$$

where the subscript $E$ referring to the Eulerian autocorrelation coefficient from measurements at a fixed point and $\beta$ is the ratio of the Lagrangian to the Eulerian time scales.

Consequently, the relation

$$\int_0^\infty {}_wR_L(\xi)d\xi=\beta\int_0^\infty {}_wR_E(t)dt \tag{3.55}$$

can be obtained.

From the observations of the crosswind spread of particles and the simultaneous measurements of the fluctuations of wind speed, they summerized the average value of $\beta$ as being 4 with a "scatter range" from 1.1 to 8.5 for the diffusion over short distances in the atmosphere.

*Baldwin and Mickelsen* (1962) have demonstrated that the parameter $\beta$ is proportional to the ratio of the mean velocity to the turbulence intensity. The error

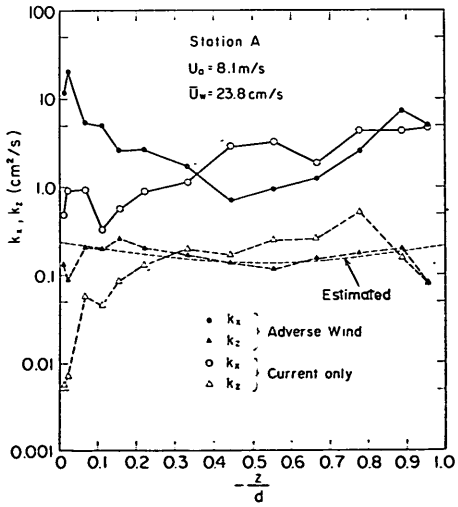


**Fig. 41** Eulerian Diffusion Coefficient (Station A, $\bar{U}_w$=23.8 cm/s)

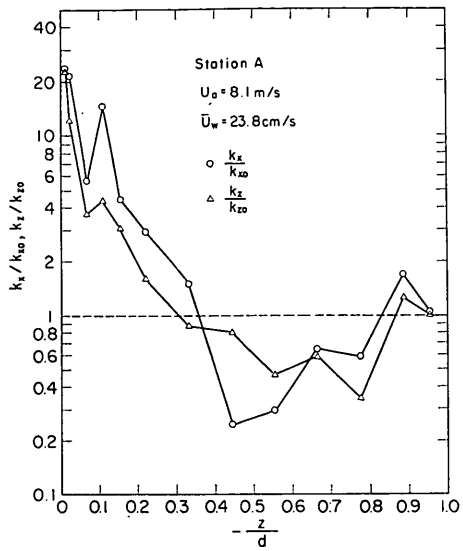


**Fig. 42** Ratio of Adverse Wind to Current Only Eulerian Diffusion Coefficient

in the estimation of $\beta$ will often not be serious. If the true value is $\beta$, and the value assumed is $\beta'$, it is easily seen that the value of $\sqrt{\overline{Z}^2}$ derived will be $(\beta'/\beta)^q$ times the true value, where $q$ will vary from zero when $T$ is small to a maximum of 0.5 when $T$ is large (*Pasquill*, 1962). Because of the reason stated above, $\beta$ is assumed as unity in the present study.

Eulerian diffusion coefficients in both longitudinal and vertical directions were calculated using Eqs. (3.53) and (3.55). The results are illustrated in Fig. 41. Near the water surface, diffusion coefficients in both $x$ and $z$ directions increase in the case of adverse wind compared with that of current only. Figure 42 shows the ratio of the diffusion coefficients $K_x$, $K_z$ in the case of adverse wind to $K_{x0}$, $K_{z0}$ in the case of current only. The ratio increase up to 20 near the surface. On the contrary, this becomes less than unity in the range of $0.3<-z/d<0.85$. The tendency is similar to the case of turbulence intensities.

Eddy diffusivity $K_z$ can be represented in terms of the mixing length $l_z$ and the root-mean-square of turbulence $\sqrt{\overline{w^2}}$, namely

$$K_z=l_z\sqrt{\overline{w^2}}. \tag{3.56}$$

In the case of adverse wind $l_z$ was nearly constant and the relative value to the water depth was $l_z/d \fallingdotseq 3.2\times10^{-3}$. Using this value as the mixing length and making use of Eqs. (3.32) and (3.56), vertical diffusion coefficient $K_z$ was calculated and is illustrated in Fig. 41 as a broken line. Diffusion coefficients for another cases are shown in Figs. A-7~A-10.

## 4. Interaction of Waves and a Turbulent Current

### 4.1 Experimental Equipments and Procedures

In this experiment, two types of waves makers were used. The locations of them are shown in Fig. 1. At the windward end of the channel, a piston type wave maker is equipped to generate regular waves of relatively long period.

A plunger type wave maker is equipped at the enlarged part of the channel. In that place, wooden walls, the distance of which is the same as that of the test section are installed.

Irregular wave signal having the shape of Bretschneider-Mitsuyasu spectrum was computed by ACOS 1000/10 digital computer system. The result was recorded on a magnetic tape in a digital form. This digital data was transformed by the D-A converter (DATAC-2000B, Iwatsu Electronic Co., Ltd.) into analog data with the time intervals of 1/128.0 s and was recorded on a cassete type data recorder (R-61, TEAC Corp.). At every experiment concerning irregular waves, this analog data recorder was used to supply a wave signal to the irregular wave controller. The irregular wave maker is driven by a low-inertia DC motor (0.77 kW) through a ball-bearing screw. The movement of the plunger is directly proportional to the input signal supplied from the analog data recorder. The maximum amplitude of the plunger movement can be easily set by setting the three digit dials.

Surface displacement was measured with a resistance-type wave gauge. Current velocities were measured with a Laser-Doppler Anemometer (LDA, DISA 55X system). A 25 mW He-Ne laser was used as a light source. The focal length of the front lens 55X58 is 600 mm and taking into consideration of the beam refraction in water, it is enough to measure the velocity at the center of the channel (75 cm from the side walls). The depth of the water was kept at 50 cm.

### 4.2 Deformation of Surface Waves

Figure 43 shows the change of the wave height of regular waves without current. The total dissipation for regular waves propagating over a distance $x$ in deep water can be expressed in terms of a damping coefficient $\Delta$ by

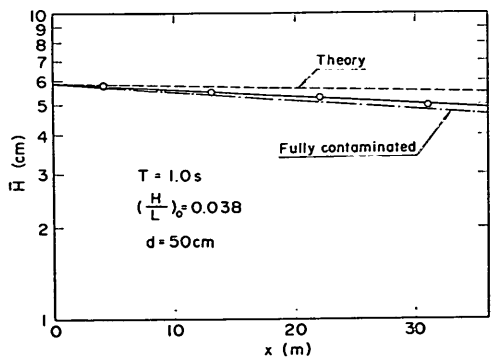


**Fig. 43** Wave Dissipation (Regular Waves, $T$=1.0 s)

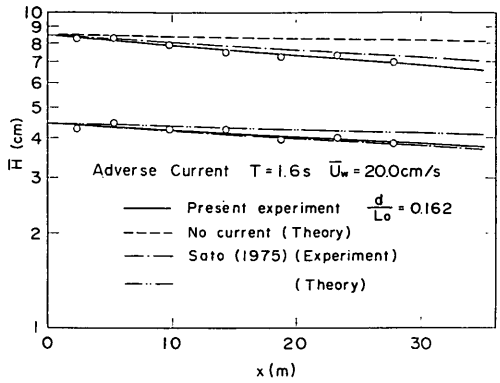


**Fig. 44** Wave Attenuations in Adverse Current (Regular Waves, $T=1.6$ s, $\bar{U}_w=20$ cm/s)

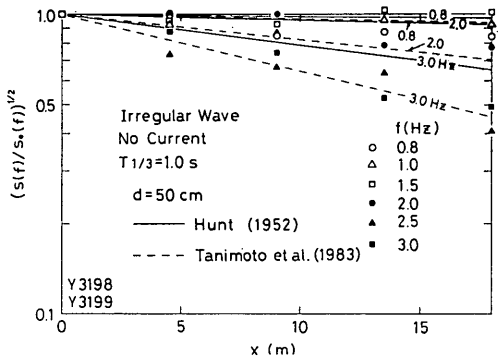


**Fig. 45** Dissipations of Irregular Wave Components ($T_{1/3}=1.0$ s)

$$H=H_0 \exp(-\Delta x), \tag{4.1}$$

where $H_0$ and $H$ are the initial and final wave heights respectively.

In a channel of uniform width $b$ and depth $d$ the damping coefficient $\Delta_b$ due to boundary dissipation at side walls and a bottom of the flume has been given by *Hunt* (1952) as

$$\Delta_b=\frac{2k}{b}\left(\frac{\nu_w}{2\omega}\right)^{\frac{1}{2}}\frac{kb+\sinh 2kd}{2kd+\sinh 2kd}, \tag{4.2}$$

where $\omega$ is an angular frequency and the relation (4.2) is shown by broken line in Fig. 43.

*Van Dorn* (1966) has investigated the surface wave damping due to the surface-film effect. Assuming the free surface to be horizontally immobilized (fully contaminated), the surface damping coefficient $\Delta_s$ can be expressed as

$$\Delta_s=\frac{2k}{b}\left(\frac{\nu_w}{2\omega}\right)^{\frac{1}{2}}\frac{kb\sinh^2 kd}{2kd+\sinh^2 kd}. \tag{4.3}$$

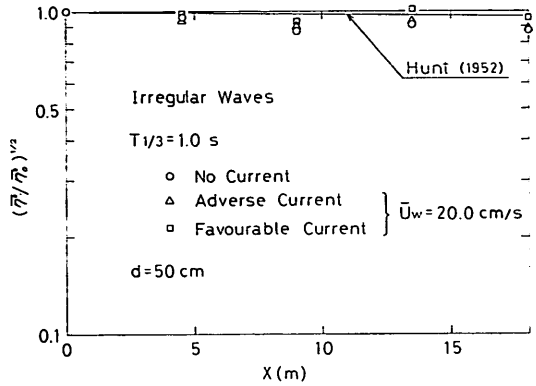


**Fig. 46** Attenuations of Irregular Waves in No Current, Adverse Current and Favourable Current Conditions

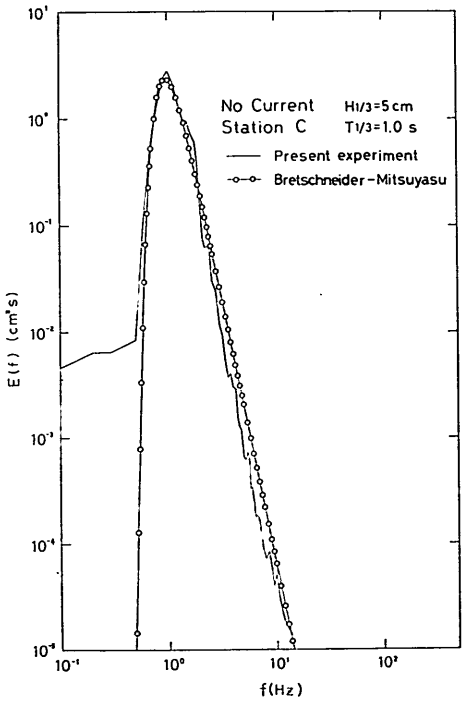


**Fig. 47** Wave Spectra (Bretschneider-Mitsuyasu and Observed Spectra)

The total change of the mean wave height by the viscous damping (4.2) and the surface damping (4.3) is shown by dash-dot line in Fig. 43. Figure 44 shows the change of the wave height of regular waves propagating on adverse current. The mean velocity of the current is 20 cm/s. *Sato* (1975) has investigated the wave damping propagating on a shear current. In his theory the influence of wave amplitude on the damping coefficient is not included. It can be read from the figure,

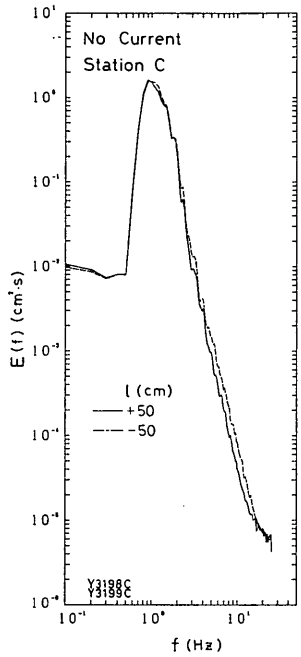


**Fig. 48** Wave Spectra (No Current)

however, that if the initial wave height is large the damping coefficient is also large. The straight lines in Fig. 44 are drawn by the least-square methods applied to the present experimental data. They agree well with *Sato's* experimental lines especially for the case of smaller wave height.

Figure 45 shows the change of the relative power of irregular wave components without current. The detailed properties of the irregular waves will be discussed later. For the higher frequency components, damping coefficients are much larger than that by viscous damping (4.2). *Tanimoto et al.* (1983) have investigated the irregular wave damping in a concrete channel. Present results are in approximate agreement with *Tanimoto's* data. Next, the change of the irregular wave heights in a current were investigated. Figure 46 shows the change of the relative total power. There is no significant difference between no current, adverse current and favourable current conditions. In the figure the straight line represents the viscous damping Eq. (4.2). In calculating Eq. (4.2), significant wave period $T_{1/3}$ was used as a representative wave period.

Figure 47 shows the power spectrum of irregular waves without current observed at station C. The observed spectrum agrees well with Bretschneider-Mitsuyasu spectrum. A correction of the operation signal of the plunger was made using the observed spectrum at station C. The spectra observed at stations lateral distances of which are 50 cm from the center of the channel to the left (+50 cm) and to the right (−50 cm) looking in the wind direction are shown in Fig. 48. Figures 49 and 50 show the wave spectra in the case of adverse current and favourable current respectively. The movement of the irregular wave maker was the same as that of the case of no current. In the case of adverse current (Fig. 49) the peak becomes sharp and large compared with that of the case without current. It will be partly

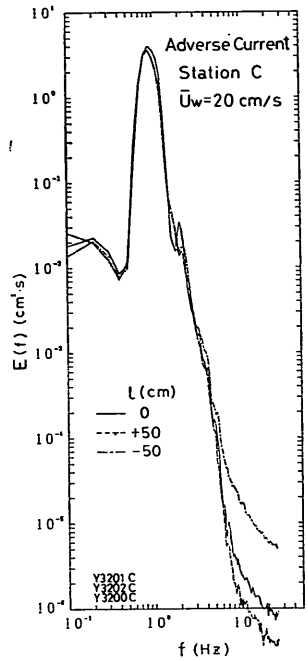


**Fig. 49** Wave Spectra Generated on Adverse Current ($\bar{U}_w$=20cm/s)

because of the increase of wave breaking of higher frequency components. On the contrary, in the case of favourable current (Fig. 50) the power near the peak slightly decreases compared with that of the case of no current. But in the higher frequency regions the power decrease rapidly the same as the case of adverse current.

Figure 51 shows the statistical properties of irregular waves without current analized by the zero-up crossing method. In the left of the figure shows a relative wave height distribution. The time of measurement is 160 s. Sampling time is $\Delta t$=1/102.4 s and the total number of discrete data points $N$ is 16384. The total number of waves is 189.

The observed data obeys a Rayleigh distribution:

$$p(x)=\frac{\pi}{2}x\exp\left(-\frac{\pi}{4}x^2\right), \qquad x=H/\bar{H}, \tag{4.4}$$

where $\bar{H}$ is the mean wave height. Probability density distribution of the relative wave period $T/\bar{T}$ can be expressed as

$$p(\tau')=\frac{\hat{\nu}^2}{2[\hat{\nu}^2+(\tau'-1)^2]^{3/2}}, \quad \tau'=T/\bar{T}, \tag{4.5}$$

(e.g., see *Goda*, 1977, p. 181).

In the middle of Fig. 51 shows the probability density distribution of the relative wave period and Eq. (4.5). The value of $\hat{\nu}$ was estimated in order to fit the observed

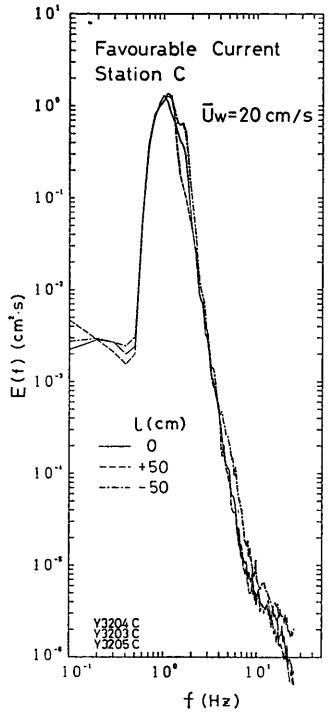


**Fig. 50** Wave Spectra Generated on Favourable Current ($\bar{U}_w$=20 cm/s)

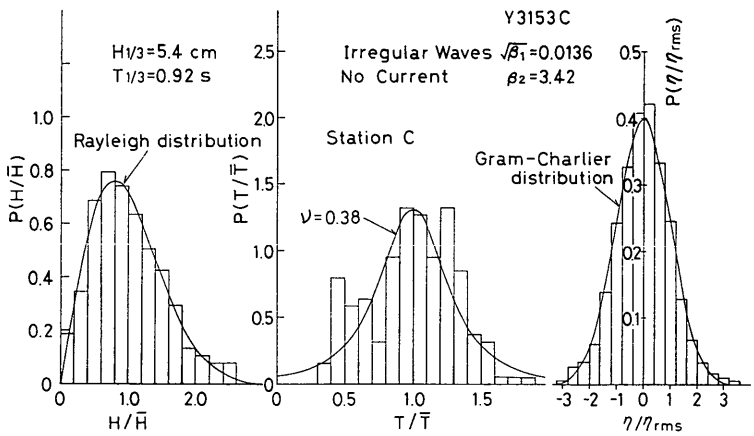


**Fig. 51** Statistical Properties of Irregular Waves (Without Current)

data. In the right of Fig. 51 shows the probability density distribution of the surface displacement. The observed data obeys a Gram-Charlier distribution:

$$p(\eta)=(2\pi m_2)^{-\frac{1}{2}}\exp\left(-\frac{1}{2}t_1^2\right)\left(1+\frac{1}{6}\sqrt{\beta}_1 H_3+\dots\right), \tag{4.6}$$

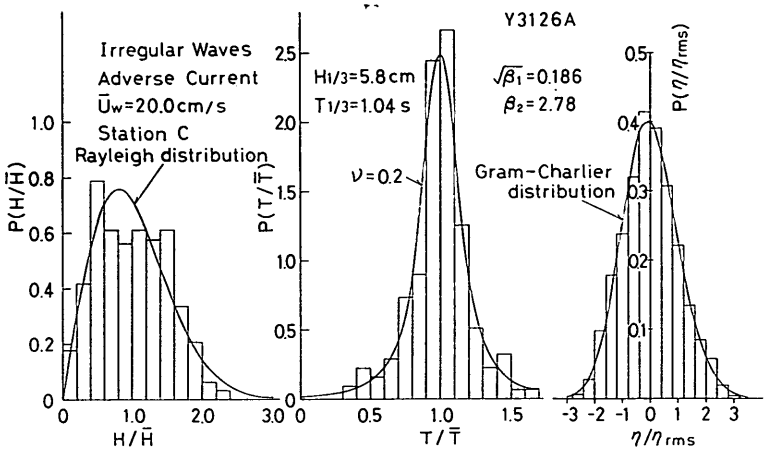


**Fig. 52** Statistical Properties of Irregular Waves (Adverse Current, $\bar{U}_w$= 20.0 cm/s)

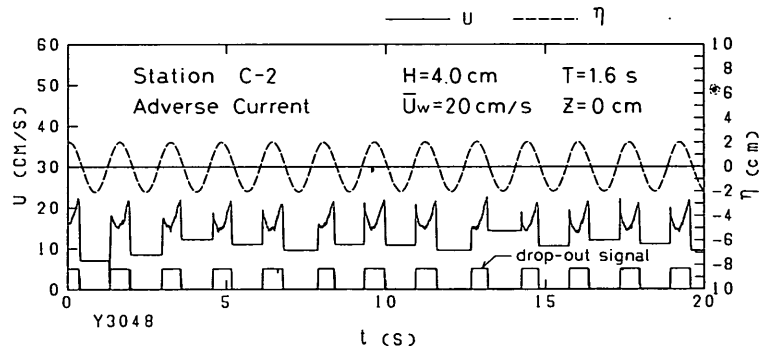


**Fig. 53** Surface Elevation and Longitudinal Velocity Component Measured at the Higher Level than the Wave Trough with LDA (Adverse Current, $T$=1.6 s, $z$=0 cm)

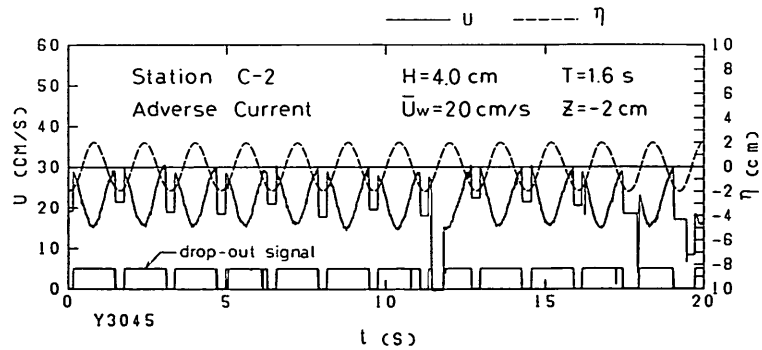


**Fig. 54** For Legend see **Fig. 53** (Adverse Current, $T$=1.6 s, $z$=−2 cm)

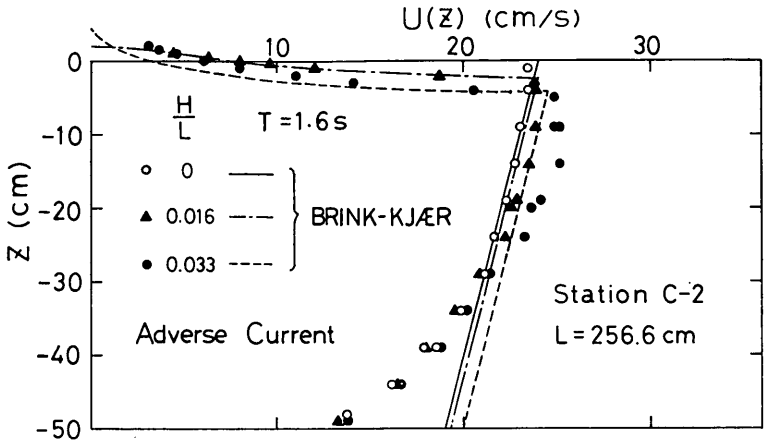


**Fig. 55** Measured Longitudinal Velocity Distribution and *BRINK-KJÆR's* Theoretical Curve

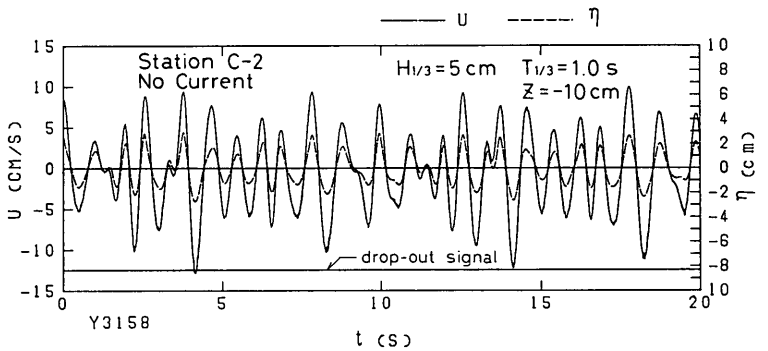


**Fig. 56** Surface Elevation and Longitudinal Velocity Component without Current

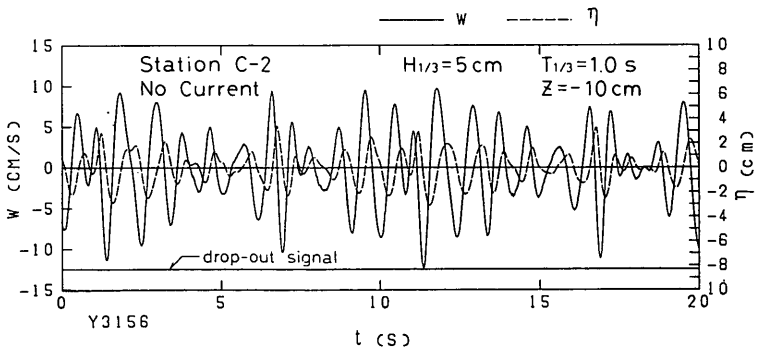


**Fig. 57** Surface Elevation and Vertical Velocity Component without Current

where $t_1=\eta/(\overline{\eta^2})^{1/2}$, $m_2=\overline{\eta^2}$, $\sqrt{\beta_1}=\overline{\eta^3}/(\overline{\eta^2})^{3/2}$ the skewness and $H_3=t_1{}^3-3t_1$ is the Hermite polinomial of degree 3 (*Phillips*, 1977). As in this case $\sqrt{\beta_1}=0.0136$ the probability distribution function (4.6) is not so different from the Gaussian distribution. Figure 52 shows the statistical properties of irregular waves generated on adverse current. The mean velocity is 20.0 cm/s. As can be considered from Fig. 49 that the spectrum has the sharp peak, the probability density distribution of the wave period has a sharp crest and the value of $\hat{\nu}$ is 0.2. This means that in this case the concentration of the wave period is very high.

### 4.3 Wave-induced Velocities and Turbulence

Making use of the piston type wave generater, regular waves were generated on adverse current. The mean velocity of the current was 20 cm/s. Velocities were measured with the LDA system at station C-2. The station C-2 is located at the middle point between stations C and D.

Figures 53 and 54 show the surface elevation $\eta$ and the velocity $U$ in the case without current with a drop-out signal at the elevation of $z=0$ cm and $-2$ cm respectively. It should be pointed out that in the case of adverse current the direction of the flow is taken to be positive.

When laser beams are scattered by the surface waves or there is no particle in the measuring volume, the output signal is locked and the drop-out signal becomes zero. In Figs. 53 and 54 when laser beams go out of the water near the trough of waves drop-out signal becomes zero. When drop-out signal is zero, output signal of the current is not taken into account.

*BRINK-KJÆR* (1976) has investigated the interaction of gravity waves and a current having the profile with a straight line. Figure 55 shows the mean velocity distributions of adverse current on which regular waves are propagating. The open circle represents the mean velocity in the case of no waves. The curves in the figure are the theoretical relations based on *BRINK-KJÆR* for the finite amplitude waves propagating on currents which have constant vorticity, i.e. the linear current profile.

Although velocity distribution cannot be approximated by the linear profile, the agreement between experimental data and the theory is good for the elevations higher than the wave trough especially when the wave slope $H/L$ is small.

Figure 56 shows the surface elevation $\eta$ and the horizontal velocity $U$ of irregular waves without current and Fig. 57 for the vertical velocity $W$.

Figures 58 and 59 show the velocities and the surface elevation in the case of adverse current. If the linear wave theory can be applied for the description of the velocity field in irregular waves, the water elevation $\eta(t)$ and the horizontal and vertical orbital velocity components $\tilde{u}$ $(t)$ and $\tilde{w}$ $(t)$ are related by

$$\begin{aligned}\tilde{u}(t)&=\int_0^\infty h_u(\tau)\{\eta(t-\tau)+\eta(t+\tau)\}\,d\tau,\\ \tilde{w}(t)&=\int_0^\infty h_w(\tau)\{\eta(t-\tau)+\eta(t+\tau)\}\,d\tau,\end{aligned}\qquad(4.7)$$

where $h_u(\tau)$ and $h_w(\tau)$ are impulse response functions. The corresponding frequency response functions are given by

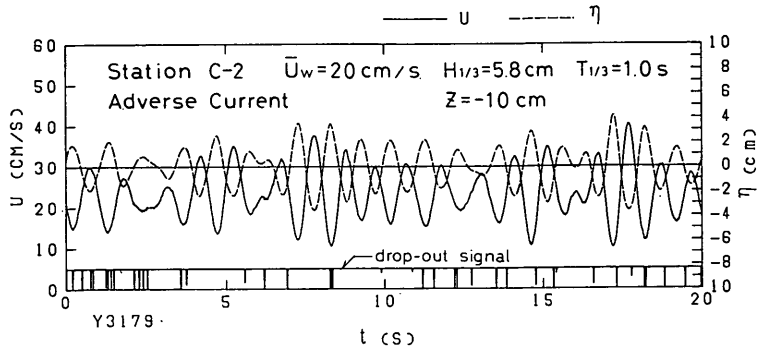


**Fig. 58** Surface Elevation and Longitudinal Velocity Component in Adverse Current

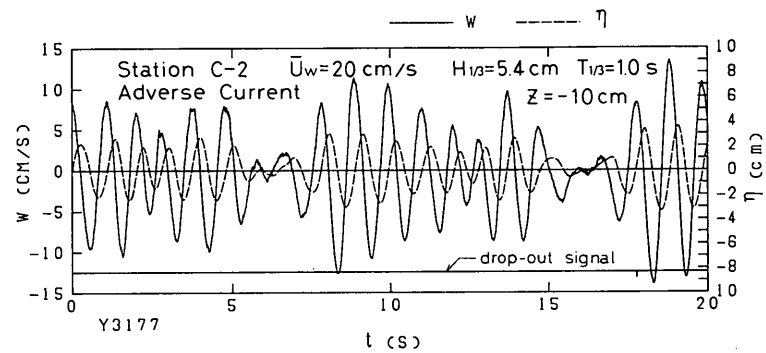


**Fig. 59** Surface Elevation and Vertical Velocity Component in Adverse Current

$$H_u(\omega)=\frac{\omega\cosh k'(d+z)}{\sinh k'd},$$
$$H_w(\omega)=i\frac{\omega\sinh k'(d+z)}{\sinh k'd}, \tag{4.8}$$

where $\omega$ $(=2\pi/T)$ is the angular frequency, $k'$ $(=2\pi/L)$ the wave number, $L$ the wave length and $d$ the water depth (*Vis*, 1980). If the water current exists, it is assumed that $\bar{U}(z)$ at the elexation $z$ is constant with respect to the waves and it can be represented as $\hat{U}$. In this case, $\omega$ can be replaced by $\omega-k'\hat{U}$ and Eq. (4.8) becomes

$$\hat{H}_u(\omega,\hat{U})=\frac{(\omega-k'\hat{U})\cosh k'(d+z)}{\sinh k'd},$$
$$\hat{H}_w(\omega,\hat{U})=i\frac{(\omega-k'\hat{U})\sinh k'(d+z)}{\sinh k'd}, \tag{4.9}$$

where $\hat{H}_u(\omega,\hat{U})$ and $\hat{H}_w(\omega,\hat{U})$ are frequency response function in the case of uniform current velocity $\hat{U}$ and $\omega-k'\hat{U}$ is the angular frequency observed from the coordinate system relative to the flow.

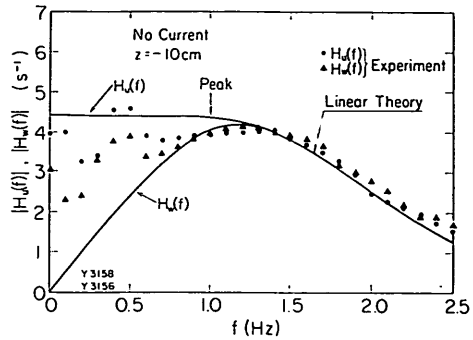


**Fig. 60** Comparison of Measured and Computed Frequency Response Function (No Current, $z=-10$ cm)

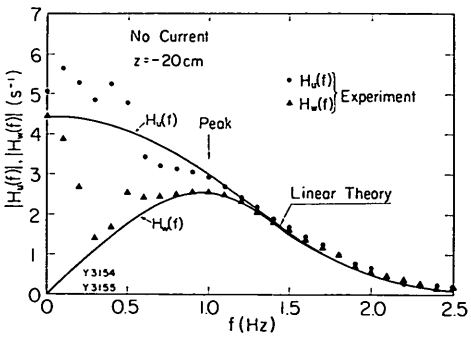


**Fig. 61** For Legend see **Fig. 60** (No Current, $z=-20$ cm)

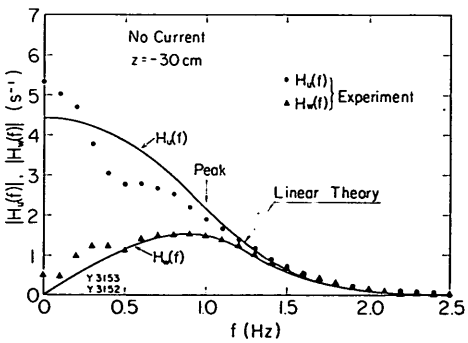


**Fig. 62** For Legend see **Fig. 60** (No Current, $z=-30$ cm)

Figures 60~62 show the measured and computed frequency response functions without current. For the frequencies higher than the peak frequency of the wave, experiental values agree well with the theoretical results. Figure 63 shows the measured and computed frequency response function in the case of adverse current. It can be seen from the figure that the linear theory hold only near the peak of the wave spectra.

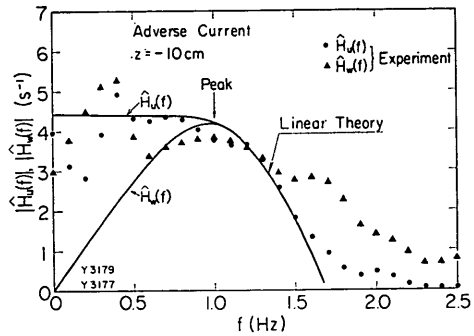


**Fig. 63** For Legend see **Fig. 60** (Adverse Current, $z=-10$ cm)

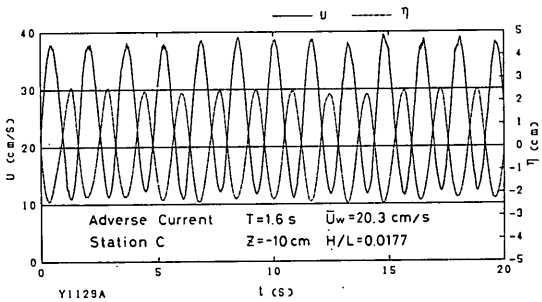


**Fig. 64** Surface Elevation and Longitudinal Velocity Component in Adverse Current (Regular waves, $T=1.6$ s)

Figure 64 shows the surface displacement $\eta$ of regular waves and the horizontal velocity $U$. The velocity was measured with a one channel fiber film prove (DISA 55R13). Frequency spectra of the velocity fluctuations were calculated for both with and without current, and they are represented in Fig. 65. Over the frequency range spectral components increase when waves exist. Except the peak and the second peak frequencies spectral densities of both cases have similar shape. In order to investigate the phase variation of turbulence, Fourier analysis was applied to the velocity fluctuations of adverse current. Fourier components higher than 2 Hz are recomposed and divided into every one period of waves and finally they were averaged to yield the ensemble mean. Figure 66 shows the ensemble mean turbulence fluctuations $\overline{u_e^2}$ and orbital velocity $\tilde{u}$. The wave period is 1.6 s and the height of the measuring point is $z=-5$ cm and mean velocity at that point is 26.4 cm/s. Turbulence components in the adverse current condition are greater than that of the no wave condition and they have the maximum value at the peak of the wave induced components which correspond to the trough of surface waves. Figure A-11 shows the turbulent fluctuations higher than the frequency of 2 Hz. The time period is 1.5 s. The phase variation of turbulence component is not remarkable. The turbulence component is much more greater than that in the current only case.

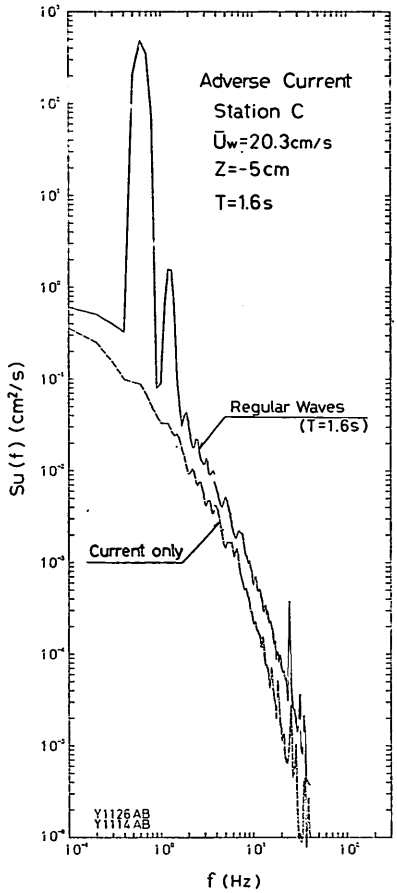


**Fig. 65** Turbulence Spectra in Adverse Current (Regular Waves, $T=1.6$ s and Current Only)

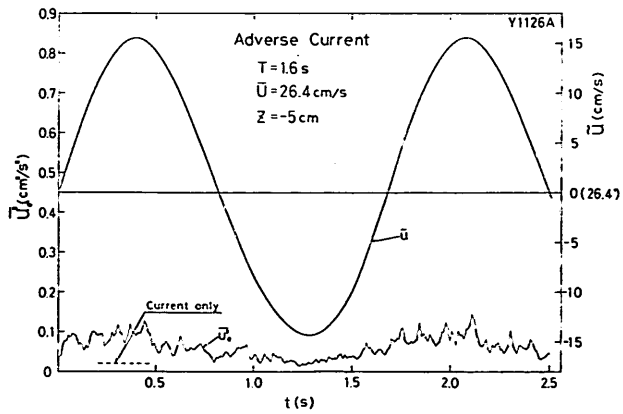


**Fig. 66** Phase Average of Turbulence Components (Frequency Components Higher than 2Hz, $T=1.6$ s)

### 4.4 Dispersion of Particles in Waves and a Turbulent Current

*G. I. Taylor* (1921) considered the diffusion of marked fluid from a point source in a field of homogeneous and stationary turbulence. The theory is called as the "one-particle analysis" and was already discussed in section 3.6. The dispersion of a transferable property by turbulent motion has been the object of many investigators. In the coastal zone, it is usual that waves and currents both exist. Moreover, the flow field is not homogenious and has the velocity gradient in the vertical direction.

In this study experiment on the dispersion of particles were conducted. The test section and the particle charging mechanism is shown in Fig. 67. The test section is located between the stations C and D. Fluid particles were made by mixing chlorobenzene ($C_6H_5Cl$) and xylene ($C_6H_4(CH_5)_2$), so as to the specific gravity becomes unity. Before the experiment the temperature of the water in the flume was measured and the specific gravity of the mixture of two liquids was checked in the water the temperature of which was the same (not differ more than 0.1°C) as the water in the flume. The boiling points of chlorobenzene and xylene are 132°C and 140°C respectively. As the boiling point is very close each other, specific gravity of the mixture kept constant for a long time. If the water temperature of the flume

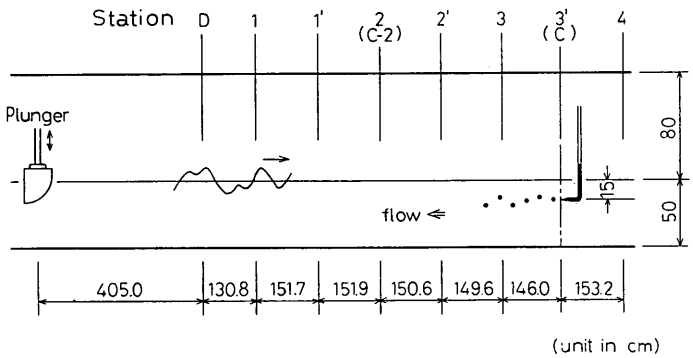


**Fig. 67** Test Section of Dispersion Experiment

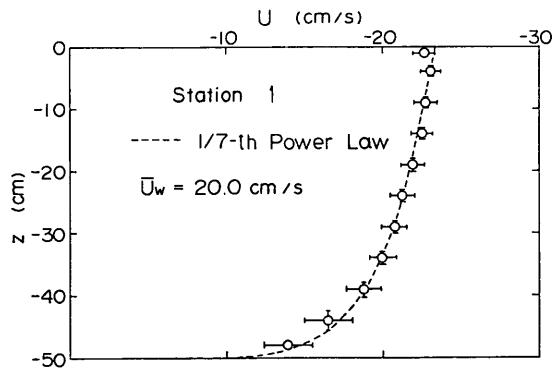


**Fig. 68** Current Profile and rms of Velocity Fluctuations (Station 1, $\bar{U}_w$=20 cm/s)

change more than 0.2°C, however, specific gravity was checked and the mixture was prepared once more.

Small particles were formed when the tracer was released from the injector which was consisted of glass pipe tapered to a point. The injection point was set at the elevation of 15 cm below the water surface at the center of the flume. At the measuring stations, vertical displacement of the specific particle was checked by eye and the distance from the initial elevation was read with the time at which the tracer had passed through the station. The diameter of the particle was about 2 mm in average.

The velocity profile at station 1 with current only case is illustrated in Fig. 68. The root-mean-square turbulence fluctuations in longitudinal and vertical directions are also shown as straight line segments in both directions. The velocity was measured with LDA. The measurements were performed with $\Delta t=1/51.2$ s and $N=8192$. The drop-out rates for the longitudinal components were ranged from 1.37% at $z=-9$ cm to 0.02% at $z=-48$ cm. In open channel flow, longitudinal turbulence fluctuations are usually greater than vertical one as we have already shown in Figs. 19 and 20. Strictly speaking, in such a situation the relatively simple approach to dispersion process in a homogeneous isotropic turbulence is no longer applicable. As a first approximation, however, the concept of isotropic turbulence is useful because of its relative simplicity.

According to *Hinze* (1962) but taking into consideration of waves, we will discuss the dispersion of a marked fluid particle starting at time $t_0$ from a point $(x_0, z_0)$ of the flow field where the turbulence flow pattern is not homogeneous.

At any time the Lagrangian velocity of the marked fluid particle is equal to the Eulerian velocity at the point that is passed by the fluid particle at the instant of passing. Namely,

$$\begin{aligned} U_p(t;\ t_0, x_0, z_0) &= \overline{U}(x, z)+\tilde{u}(t, x, z)+u(t, x, z), \\ W_p(t;\ t_0, x_0, z_0) &= \overline{W}(x, z)+\tilde{w}(t, x, z)+w(t, x, z), \end{aligned} \tag{4.10}$$

where $U_p$ and $W_p$ are the Lagrangian particle velocity, $\overline{U}$, $\overline{W}$ $(=0)$ the Eulerian mean velocity components, $\tilde{u}$, $\tilde{w}$ the wave-induced velocity components and $u$, $w$ are the turbulence velocity components at the point $(x, z)$ passed by the fluid particle at time $t$.

Consider the displacement of the fluid particle $(X(t), Z(t))$ from the initial position $(x_0, z_0)$. The position of the fluid particle at time $t$ is, then

$$\begin{aligned} x(t) &= x_0+X(t), \\ z(t) &= z_0+Z(t). \end{aligned} \tag{4.11}$$

On the other hand, the values of $X$ and $Z$ are given by the Lagrangian notation:

$$\begin{aligned} X(t;\ t_0, x_0, z_0) &= \int_{t_0}^{t} U_p(t';\ t_0, x_0, z_0)dt', \\ Z(t;\ t_0, x_0, z_0) &= \int_{t_0}^{t} W_p(t';\ t_0, x_0, z_0)dt'. \end{aligned} \tag{4.12}$$

Notice that the particle velocities $U_p$ and $W_p$ are not stationary random functions of time, since $\overline{U}\,(x, z)$ and $\tilde{u}\,(t, x, z)$ and $\tilde{w}\,(t, x, z)$ vary with time because the

coordinates $x$ and $z$ of the particle vary randomly with time.

In a flow field where surface gravity waves are propagating, the flow cannot be considered as steady. Then the average displacement at time $t$ can be represented as

$$\begin{aligned}\overline{X}(t;\ t_0, x_0, z_0)&=\int_{t_0}^{t}\overline{U_p}(t';\ t_0, x_0, z_0)dt',\\ \overline{Z}(t;\ t_0, x_0, z_0)&=\int_{t_0}^{t}\overline{W_p}(t';\ t_0, x_0, z_0)dt',\end{aligned}\tag{4.13}$$

where $\overline{U_p}$ and $\overline{W_p}$ are the ensemble average values of the Lagrangian velocity components.

In the $x$-direction, the dispersion of the fluid particles about their average displacement is

$$\begin{aligned}\overline{D_x^2}(t;\ t_0, x_0, z_0)&=\overline{[X(t;\ t_0, x_0, z_0)-\overline{X}(t;\ t_0, x_0, z_0)]^2}\\ &=2\int_0^t\int_0^{t''}\overline{[U_p(t';\ t_0, x_0, z_0)-\overline{U_p}(t';\ t_0, x_0, z_0)][U_p(t'';\ t_0, x_0, z_0)}\\ &\quad-\overline{\overline{U_p}(t'';\ t_0, x_0, z_0)}]dt'dt''.\end{aligned}\tag{4.14}$$

Similarly for the dispersion in the $z$-direction

$$\begin{aligned}&\overline{D_z^2}(t;\ t_0, x_0, z_0)\\ &=2\int_0^t\int_0^{t''}\overline{[W_p(t';\ t_0, x_0, z_0)-\overline{W_p}(t';\ t_0, x_0, z_0)][W_p(t'';\ t_0, x_0, z_0)}\\ &\quad-\overline{\overline{W_p}(t'';\ t_0, x_0, z_0)}]dt'dt''.\end{aligned}\tag{4.15}$$

In practice the flow field where waves and a turbulent current coexist is so complicated that we assume that for long time of dispersion the contribution from waves can be neglected and the flow can be regarded as approximately steady.

If the flow is steady, the average displacement does not depend on the time $t_0$, but only on the initial position $(x_0, z_0)$ and the elapse of time $t-t_0$. Without loss of generarity we can take $t_0$ as zero. Then, the average displacement and particle velocity in Eqs. (4.14) and (4.15) do not depend on $t_0$. Furthermore, if the turbulent flow is homogeneous and with a constant mean velocity, then the velocities of the fluid particles are stationary functions of time.

Let $\overline{U}$=constant and $\overline{W}=0$, we obtain from Eq. (4.10) by the assumption

$$\overline{U_p}=\overline{U} \text{ and } \overline{W_p}=0.\tag{4.16}$$

From Eq. (4.13) we obtain for the average displacement

$$\overline{X}(t)=\overline{U}t \text{ and } \overline{Z}=0.\tag{4.17}$$

Introducing the Lagrangian correlation coefficients

$$\begin{aligned}{}_uR_L(\tau)&=\frac{\overline{u_L(t)u_L(t-\tau)}}{{u_L'}^2},\\ {}_wR_L(\tau)&=\frac{\overline{w_L(t)w_L(t-\tau)}}{{w_L'}^2},\end{aligned}\tag{4.18}$$

where $u_L'=\sqrt{\overline{u_L^2}}$, $w_L'=\sqrt{\overline{w_L^2}}$ and $\tau=t'-t''$,

the expressions (4.14) and (4.15) reduce to

$$\overline{D_x^2}=\overline{(X-\bar{X})^2}=2\overline{u_L^2}\int_0^t(t-\tau)_u R_L(\tau)d\tau, \tag{4.19a}$$

$$\overline{D_z^2}=\overline{(Z-\bar{Z})^2}=2\overline{w_L^2}\int_0^t(t-\tau)_w R_L(\tau)d\tau. \tag{4.19b}$$

Equation (4.19) is analogous to Eq. (3.48).

Next, we consider the dispersion in a homogeneous shear flow. The flow is assumed to be an unbounded homogeneous parallel isotropic turbulent flow with a mean velocity in the $x$ direction and which has a constant gradient $d\overline{U}/dz$.

For the case of $\overline{U}=0$ at $z=-d$, and for very short diffusion times so that the Lagrangian correlation coefficients are approximately equal to unity, *Hinze* obtained the dispersions of the fluid particles as

$$\overline{X^2}(t)\fallingdotseq u_L'^2t^2+\frac{8}{15}w_L'^2\left(\frac{d\overline{U}}{dz}\right)t^4, \tag{4.20a}$$

$$\overline{Z^2}(t)\fallingdotseq w_L'^2t^2. \tag{4.20b}$$

In this experiment dispersion of neutral buoyant particles was examined in the field where waves and a current coexist. In most cases the number of the particles used was from 30 to 40. When the wave amplitude becomes great, however, some particles reach the water surface. In this case the number of observed particles is decreased to about 25.

The mean-squared displacements $\overline{D_x^2}(t)$ and $\overline{D_z^2}(t)$ in $x$ and $z$ direction are shown in Figs. 69 and 70 respectively. Theoretical relation (3.49) is also shown in the figures, assuming that the Lagrangian and Eulerian turbulence intensities are equal. In Fig. 69 theoretical relation in a shear flow (4.20a) is also illustrated.

From the figures, we can admit the Taylor's theory (3.49) and (3.50), that is, for the early stage, the dispersion is proportional to the square of the time and later it is directly proportional to the time. The asterisks in Fig. 70 are the data read from the photos in order to check the accuracy of the data in the current only condition. In the photos, from 139 to 239 particles were read. The despersions read

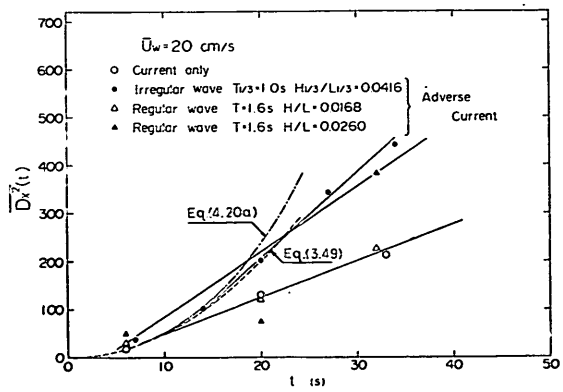


**Fig. 69** Longitudinal Dispersion of Particles

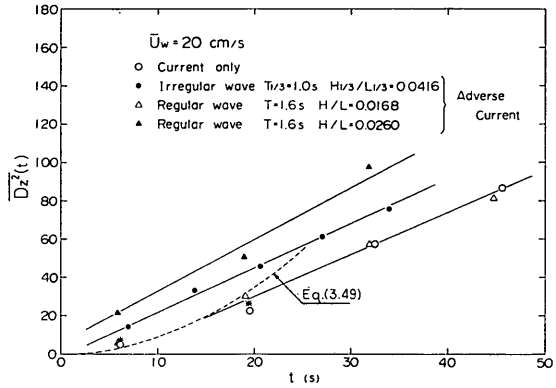


**Fig. 70** Vertical Dispersion of Particles

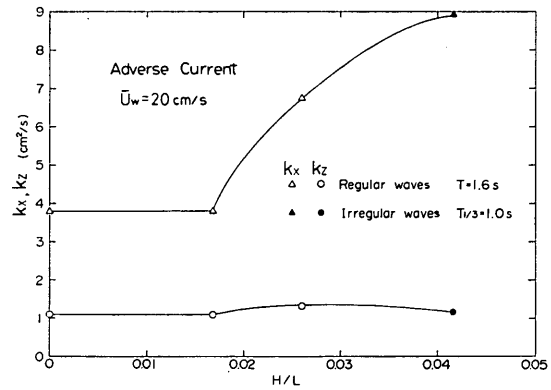


**Fig. 71** Diffusion Coefficients in Adverse Current Fields

by eye and from the photos are nearly equal.

When the wave slope is small ($H/L=0.0168$) mean-squared displacements in both $x$ and $z$ directions do not change compared with the case of current only. As the wave slope becomes large the slope of $\overline{D_x}^2(t)$ becomes also large, but the slope of $\overline{D_z}^2(t)$ does not change appreciably. When wave motions exist the turbulent flow field cannot be considered as homogeneous and stationary. It is asumed, however, that Taylor's one-particle analysis can hold for a long period of observation. Then we can evaluate the diffusion coefficient from Eq. (3.52). Estimated diffusion coefficients are shown in Fig. 71. It can be said from the figure that as the wave slope become large, the diffusion coefficient in the $x$ direction rize suddenly. The diffusion coefficients in the $z$ direction, on the contrary, scarcely change with the wave slope.

## 5. Conclusions

Turbulent fluctuations and velocity profiles were measured in the flow field under the action of wind by using a V-type hot-film anemometer. Contributions of wind

to the turbulent structures and velocity profiles were discussed together with the Eulerian diffusion coefficient.

In order to investigate the interaction of waves and a current, a plunger type irregular wave maker and a piston type regular wave maker were used. Diffusion experiment was also performed using small neutral buoyant particles.

The following conclusions can be drawn from the present study:

1. When wind blows over the adverse current, turbulent fluctuations and diffusion coefficients in both longitudinal and vertical components increase near the water surface. On the contrary, they decrease near the central region of the flow. The reason become clear from the experiment in which waves were suppressed by adding detergent. According to this experiment the mean velocity profile is deformed by wind shear. Consequently in the case of adverse current, a gradient of velocity profile vanish near the center of the flow and turbulent production by the Raynolds stress also vanish causing the decrease of turbulence intensities and diffusion coefficient.
2. Mean velocity profile of adverse current under the action of wind can be approximately represented by both Reid's theory and author's experimental equation.
3. The way to predict the turbulent intensities and diffusion coefficient in the adverse current under the action of wind have been proposed.
4. Velocity distribution above the level of the wave trough was measured by LDA in adverse current conditions. It can be well explained by the finite amplitude theory when wave steepness is small.
5. Linear response function of wave orbital velocity in the current have been derived. According to this theory and experimental data of irregular waves propagating in adverse current, linear theory can hold only near the peak frequency of irregular waves.
5. It is found from the diffusion experiment in which waves propagate against the current, that with the increase of wave steepness longitudinal diffusion coefficient also increase, but vertical diffusion coefficient does not appreciably.

**Acknowledgements**

The authors wish to thank *Dr. Y. Goda*, the Deputy Director General, for his critical reading of the manuscript and valuable comments. The authors also wish to express their appriciation to *Mr. S. Nakano*, member of Hydrodynamics Laboratory, for his valuable discussions and the typing of the manuscript, and to *Mr. H. Ichinohe*, member of Hydrodynamics Laboratory, for drawing the figures.

(*Recieved on September 29, 1984*)

## References

1) BALDWIN, L. V. and MICKELSEN, W. R. (1962): Turbulent diffusion and anemometer measurements. *Proc. ASCE, J. Eng. Mech. Div.*, Vol. 88, No. EM2, pp. 37–69.
2) BRADSHAW, P. (1967A): 'Inactive' motion and pressure fluctuations in turbulent boundary layers. *Jour. Fluid Mech.*, Vol. 30, pp. 241–258.
3) BRADSHAW, P. (1967B): Conditions for the existence of an inertial subrage in turbulent flow. *N.P.L., Aero. Rept.*, No. 1220, pp. 1–5.
4) BRINK-KJÆR, O. (1976): Gravity waves on a current: the influence of vorticity, a sloping bed, and dissipation. *Series Paper No. 12, Technical Univ. of Denmark*, 137 p.

5) GODA, Y. (1977): *Design of Harbour Structure against Random Seas —Introduction to Ocean Wave Engineering— (in Japanese)*. Kajima Pub. Soc., Tokyo.
6) GRANT, H. L., STEWART, R. W. and MOILLIET, A. (1962): Turbulent spectra from a tidal channel. *Jour. Fluid Mech.*, Vol. 12, pp. 241–268.
7) HAY, J. S. and PASQUILL, F. (1957): Diffusion from a fixed source at a height of a few hundred feet in the atmosphere. *Jour. Fluid Mech.*, Vol. 2, Part 3, pp. 299–310.
8) HAY, J. S. and PASQUILL, F. (1959): Diffusion from a continuous source in relation to the spectrum and scale of turbulence. Atmospheric diffusion and air pollution, *Advances in Geophysics*, Vol. 6, pp. 345–365, Academic Press.
9) HINZE, J. O. (1962): Dispersion in turbulent shear-flow. *Mecanique de la turbulence, Colloques Internaux du Centre National de la Recherche Scientifique*. pp. 63–76.
10) HINZE, J. O. (1975): *Turbulence, 2nd ed.*, McGraw-Hill.
11) HONDA, T. and MITSUYASU, T. (1980): Experimental study of the effects of wind shear on the water surface (*in Japanese*). *Proc. 27th Japanese Conf. Coastal Engg.*, Japanese Soc. Civil Eng., pp. 90–93.
12) HUNT, J. W. (1952): Viscous damping of waves over an inclined bed in a channel of finite width. *La Houille Blanche*, Vol. 7, pp. 836–842.
13) IMAMOTO, H. (1977): The structure of turbulence in free surface shear flow (*in Japanese*). *Disaster Prev. Res. Inst. Annu.*, Kyoto Univ., No. 20A, pp. 29–48.
14) INOUE, E. (1950): On the smallest turbulon in a turbulent fluid (*in Japanese*). *Rept. Inst. Sci. and Tech.*, Univ. of Tokyo, Vol. 4, No. 7・8, pp. 194–200.
15) KEMP, P. H. and SIMONS, R. R. (1982): The interaction between waves and a turbulent current: waves propagating with the current. *Jour. Fluid Mech.*, Vol. 116, pp. 227–250.
16) KEMP, P. H. and SIMONS, R. R .(1983): The interaction of waves and turbulent current: waves propagating against the current. *Jour. Fluid Mech.*, Vol. 130, pp. 73–89.
17) LU, S. S. and WILLMARTH, W. W. (1973): Measurements of the structure of the Reynolds stress in a turbulent boundary layer. *Jour. Fluid Mech.*, Vol. 60, pp. 481–511.
18) MCQUIVEY, R. S. and RICHARDSON, E. V. (1969): Some turbulence measurements in open-channel flow. *Proc. of ASCE*, HY-1, pp. 209–223.
19) MONTGOMERY, R. B. (1943): Generalization for cilinders of Prandtl's linear assumption for mixing length. *Annals N. Y. Academy of Sciences*, Vol. 44, Art. 1.
20) NEZU, I. (1977): *Basic research on the turbulent structure of open channel flow (in Japanese)*. Doctral thesis presented to Kyoto University, 118 p.
21) PANOFSKY, H. A. and DUTTON, J. A. (1983): *Atmospheric Turbulence*, John Wiley & Sons.
22) PASQUILL, F. (1962): *Atmospheric diffusion*. D. van Nostrand Company Ltd.
23) PEREGRINE, D. H. (1976): Interaction of water waves and currents. *Advances in Appl. Mech.*, Vol. 16, Academic Press, pp. 9–117.
24) PEREGRINE, D. H. and JONSSON, I. G .(1983): Interaction of waves and currents. *Miscellaneous Rept.* No. 83–6, U.S. Army, Corps of Eng., 88 p.
25) PHILLIPS, O. M. (1977): *The Dynamics of the Upper Ocean*, 2nd ed., Cambridge Univ. Press.
26) REID, R. O. (1957): Modification of the quadratic bottom-stress law for turbulent channel flow in the presence of surface wind-stress. *Technical Memo.*, No. 93, Beach Erosion Board, Corps of Eng., 33 p.
27) SATO, M. (1975): A basic study on the changes in height of waves on opposing non-uniform current (*in Japanese*). *Proc. JSCE*, No. 242, pp. 15–29.

28) TANIMOTO, K., TOMIDA, E. and MURANAGA, T. (1983): Influence of reflection from a wave paddle on irregular incident waves (*in Japanese*). *Tech. Note Port and Harbour Res. Inst.*, No. 467, 23 p.

29) TAYLOR, G. I. (1921): Diffusion by continuous movements. *Proc. London Math. Soc.* Ser. 2, Vol. 20, pp. 196–212.

30) TSURUYA, H., NAKANO, S., KATO, H. and ICHINOHE, H. (1983): Experimental study of wind driven currents in a wind-wave tank —Effect of return flow on wind driven currents— (*in Japanese*). *Rept. Port and Harbour Res. Inst.*, Vol. 22, No. 2, pp. 127–174.

31) VAN DORN, W. G. (1966): Boundary dissipation of oscillatory waves. *Jour. Fluid Mech.* Vol. 24, part 4, pp. 769–779.

32) VAN HOFTEN, J. D. A. and KARAKI, S. (1976): Interaction of waves and a turbulent current. *Proc. 15th Int. Conf. Coastal Engg.*, Honolulu, pp. 404–442.

33) VIS, F. C. (1980): Orbital velocities in irregular waves. *Water. Lab. Delft Hydraulics Lab.*, No. 231, 13 p.

34) YANO, M. and YAMAZAKI, H. (1977): Turbulent diffusion in the field of wind waves and a current (*in Japanese*). *Proc. 24th. Japanese Conf. Coastal Egg.*, Japanese Soc. Civil Eng., pp. 514–518.

35) ZAGUSTIN, A. and ZAGUSTIN, K. (1969): Analytical solution for turbulent flow in pipes. *La Houille Blanche*, No. 2, pp. 113–118.

## List of Symbols

$A$ : absolute constant (=0.47)
$B_0$ : $\sqrt{|(1-m)r_0-m|}$
$B_1$ : $\sqrt{|1+(1-m)r_1|}$
$b$ : channel width
$C$ : concentration of the property undergoing diffusion
$D_{i,H'}$ : indicator function
$D_x^2$ : dispersion of particles in $x$ direction
$D_z^2$ : dispersion of particles in $z$ direction
$D_1$ : constant (=2.30)
$D_2$ : constant (=1.27)
$d$ : water depth
$E(f)$ : frequency spectrum of waves
$F$ : flux of the property across a fixed surface
$f$ : frequency
$f_c$ : cut-off frequency
$G_{1b}$ : constant (Eq. 3.32)
$G_{1w}$ : constant (Eq. 3.32)
$G_{2b}$ : constant (Eq. 3.32)
$G_{2w}$ : constant (Eq. 3.32)
$H$ : wave height
$H_u(\omega)$ : frequency response function for $u$ component
$H_w(\omega)$ : frequency response function for $w$ component
$H_0$ : initial wave height
$H_3$ : Hermite polinomial of degree 3
$\bar{H}$ : mean wave height
$H'$ : hole size
$h_u(\tau)$ : impulse response function for $u$ component
$h_w(\tau)$ : impulse response function for $w$ component
$K(T)$ : diffusion coefficient
$K_x$ : longitudinal diffusion coefficient
$K_{x0}$ : longitudinal diffusion coefficient in the case of current only
$K_z$ : vertical diffusion coefficient
$K_{z0}$ : vertical diffusion coefficient in the case of current only
$k$ : wave number of flow ($=2\pi f/U$)
$k_d$ : ($=1/\eta$)
$k'$ : wave number of waves ($=2\pi/L$)
$k*$ : upper limit of integration (Ep. 3.41)
$L$ : wave length
$l$ : mixing length
$l_z$ : mixing length of diflusion in $z$ direction
$m$ : ratio of bottom stress to surface stress ($=\tau_b/\tau_s$)
$m_2$ : mean square of surface displacement
$N$ : total number of the data used in a computation
$p$ : pressure
$R$ : radius of the pipe
${}_uR_L$ : longitudinal Lagrangian aut-correlation coefficient
${}_wR_E$ : vertical Eulerian auto-correlation coefficient

$_wR_L$ : vertical Lagrangian auto-correlation coefficient
$R_{e1}$ : Reynolds number($=\sqrt{\overline{u^2}}\,\lambda_E/\nu$)
$r$ : radial distance measured from the axis of the pipe
$r_0$ : relative roughness length for the channel bed ($z_{0b}/d$)
$r_1$ : relative roughness length for the free surface ($=z_{0w}/d$)
$S(k)$ : wave number spectrum of turbulence
$S_{i,H'}$ : contribution rate from $i$-th quadrant to the Reynolds stress
$S_u(k)$ : wave number spectrum of $u$ component
$S_w(k)$ : wave number spectrum of $w$ component
$S_0$ : typical power $(=\varepsilon\nu_w{}^5)^{1/4}$
$T_{i,H'}$ : fraction of time
$T_L$ : constant time-scale of turbulence
$T_{1/3}$ : significant wave period
$U(z)$ : longitudinal current velocity
$U_a$ : free stream wind velocity
$U_a(z)$ : wind speed at an elevation $z$
$U_m$ : longitudinal relative current velocity at $\zeta=\zeta_m$ (maximum relative velocity for the case of negative $m$)
$U_p$ : longitudinal partice velocity
$\overline{U}(z)$ : longitudinal mean velocity at height $z$
$\overline{U}_w$ : mean velocity of the section
$u$ : longitudinal (streamwise) turbulence velocity fluctuations
$u_L$ : Lagrangian longitudinal velocity fluctuations
$\tilde{u}$ : longitudinal wave-induced velocity fluctuations
$u'$ : longitudinal root-mean-square turbulence velocity component ($\sqrt{\overline{u^2}}$)
$u_L'$ : Lagrangian longitudinal root-mean-square turbulence velocity component
$u_0$ : surface velocity
$\overline{u_e^2}$ : ensemble averaged turbulence components higher frequencies than 2 Hz
$u_*$ : friction velocity of the flow
$u_{*a}$ : friction velocity of air ($=\sqrt{\tau_a/\rho_a}$)
$u_{*b}$ : friction velocity at the bottom ($=\sqrt{\tau_b/\rho_w}$)
$u_{*w}$ : friction velocity of the stream at the free surface
$v$ : turbulent velocity fluctuations in $y$ direction perpendicular to $x$-$z$ axis
$W(z)$ : vertical current velocity
$W_p$ : vertical particle current velocity
$\overline{W}$ : vertical mean velocity
$w$ : vertical turbulence velocity fluctuations
$w_L$ : Lagrangian vertical velocity fluctuations
$\tilde{w}$ : vertical wave-induced velocity fluctuations
$w'$ : vertical root-mean-square turbulence-velocity component ($\sqrt{\overline{w^2}}$)
$w_L'$ : Lagrangian vertical root-mean-square turbulence-velocity component
$X$ : horizontal displacement of the fluid particle
$x$ : horizontal axis
$x_0$ : $x$ component of initial position
$y$ : $=\sqrt{|m+(1-m)\zeta|}$
$Z$ : vertical displacement of the fluid particle
$z$ : height above the mean water surface
$z_0$ : $z$ component of initial position
$z_{0a}$ : roughness length of water surface for wind

$z_{0b}$ : roughness length for the channel bed
$z_{0w}$ : roughness length for the free surface in water
$\overline{\quad}$ : upper bar denoting overall time average
$< >$ : conditional sampling
$\alpha$ : Heisenberg constant in relation to the eddy viscosity
$\beta$ : ratio of the Lagrangian to Eulerian time scale
$\beta'$ : assumed value of $\beta$
$\sqrt{\beta_1}$ : skewness of surface elevation
$\Delta$ : damping coefficient
$\Delta_b$ : damping coefficient due to boundary dissipation at side walls and a bottom
$\Delta_s$ : surface damping coefficient
$\Delta t$ : data sampling time interval
$\varepsilon$ : dissipation rate by turbulence per unit mass
$\zeta$ : relative height measured from the bottom $(=(d+z)/d)$
$\zeta_m$ : height where shear stress vanishes $(=|m|/(1+|m|))$
$\eta$ : Kolmogoroff length scale
$\kappa$ : von Kármán constant $(=0.4)$
$\kappa'$ : modified von Kármán constant $(=\kappa(1+r_0+r_1))$
$\lambda$ : constant $(=2.0)$
$\lambda_E$ : Taylor's microscale
$\lambda_1$ : constant (Eq. 3.33)
$\lambda_2$ : constant (Ep. 3.33)
$\lambda_1'$ : constant (Ep. 3.32)
$\lambda_2'$ : constant (Ep. 3.32)
$\nu$ : kinematic viscosity of fluid
$\nu_a$ : kinematic viscosity of air
$\nu_w$ : kinematic viscosity of water
$\hat{\nu}$ : parameter showing the bandwidth of spectrum (cf. Eq. (4.5))
$\rho$ : density of fluid
$\rho_a$ : density of air
$\rho_w$ : density of water
$\tau$ : shear stress within the flow
$\tau_a$ : wind shear stress at the water surface
$\tau_b$ : shear stress at the bottom
$\tau_s$ : shear stress at the free surface
$\omega$ : angular frequency of waves $(=2\pi f)$

## Appendix

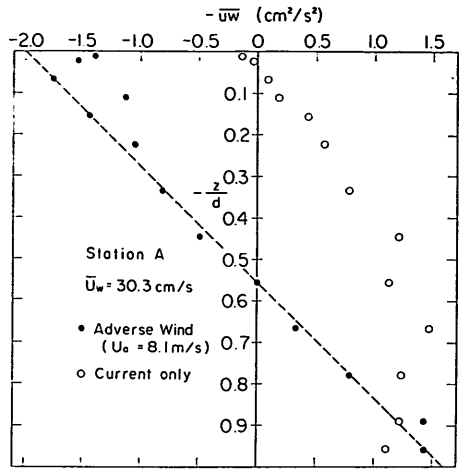


**Fig. A-1** Reynolds Stress (Station A, $\bar{U}_w = 30.3$ cm/s)

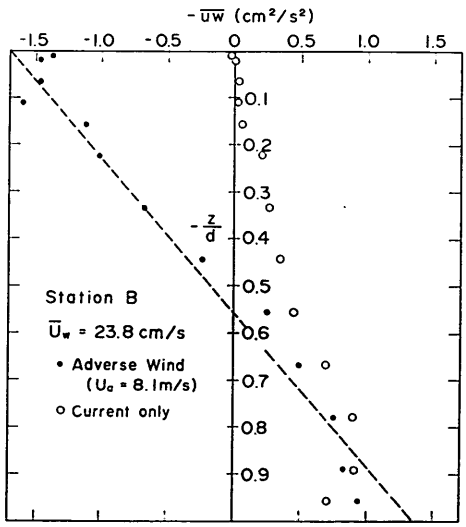


**Fig A-2** Reynolds Stress (Station B, $\bar{U}_w = 23.8$ cm/s)

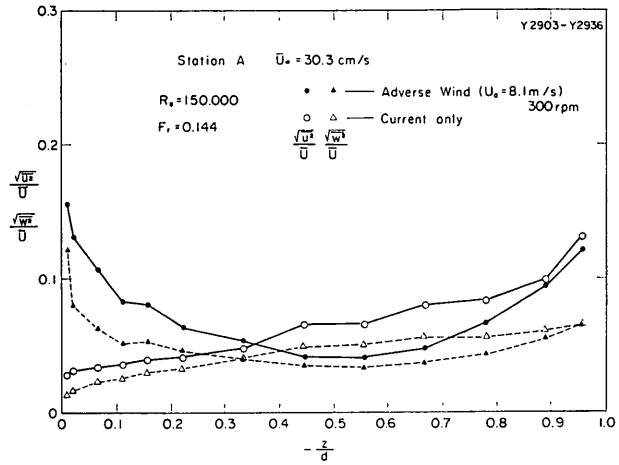


**Fig. A-3** Turbulence Intensities (Station A, $\bar{U}_w$=30.3 cm/s)

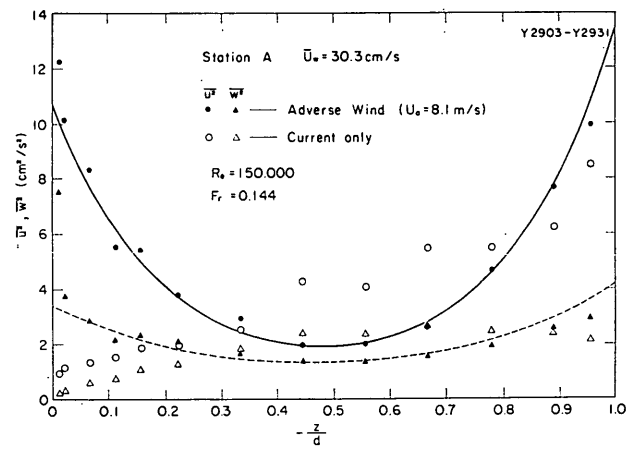


**Fig. A-4** Mean Square Values of Velocity Fluctuations (Station A, $\bar{U}_w$=30.3 cm/s)

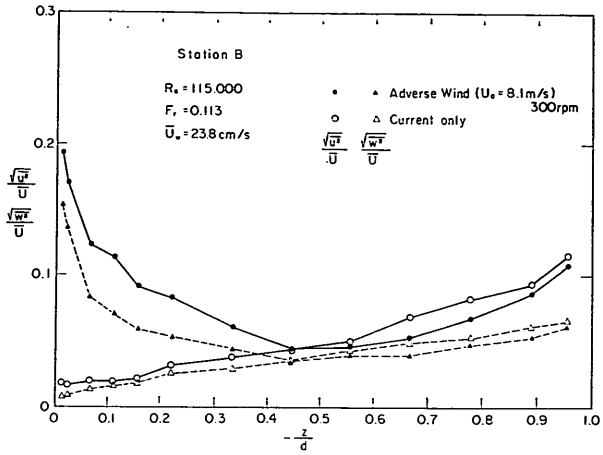


**Fig. A-5** Turbulence Intensities (Station B, $\bar{U}_w$=23.8 cm/s)

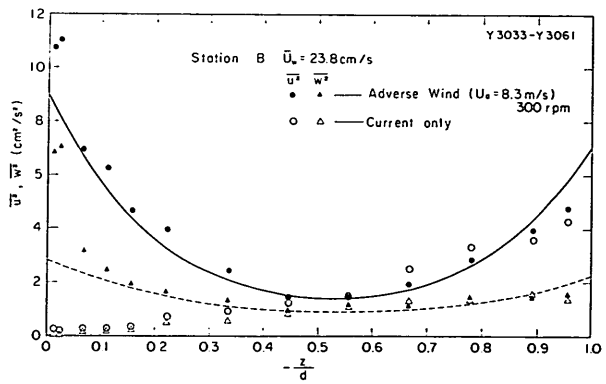


**Fig. A-6** Mean Square Values of Velocity Fluctuations (Station B, $\bar{U}_w$=23.8 cm/s)

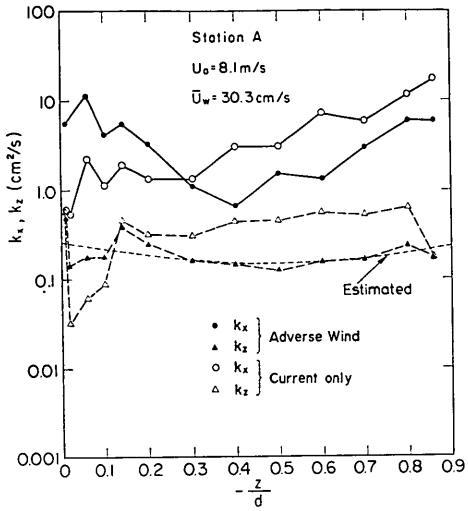


**Fig. A-7** Eulerian Diffusion Coefficient (Station A, $\bar{U}_w$=30.3 cm/s)

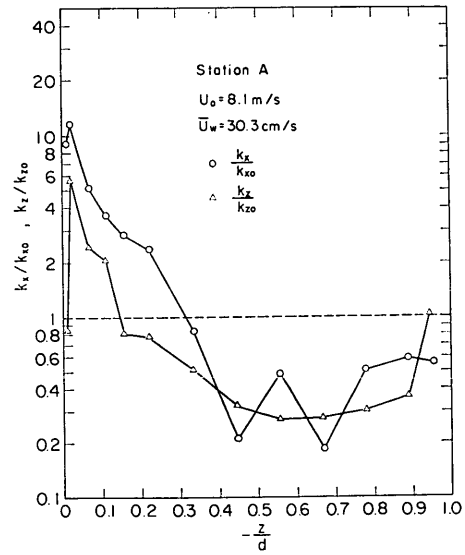


**Fig. A-8** Ratio of Adverse Wind to Current Only Eulerian Diffusion Coefficient (Station A, $\bar{U}_w$=30.3 cm/s)

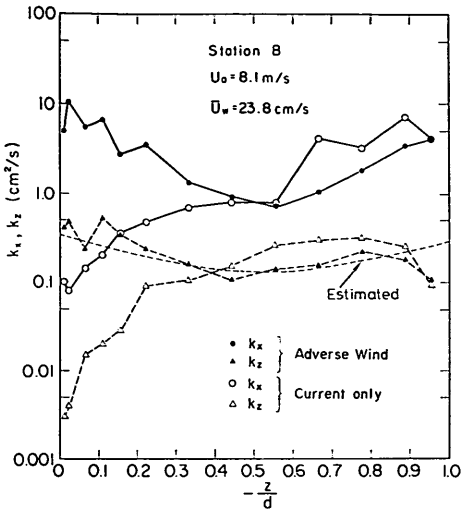


**Fig. A-9** Eulerian Diffusion Coefficient (Station B, $\bar{U}_w = 23.8$ cm/s)

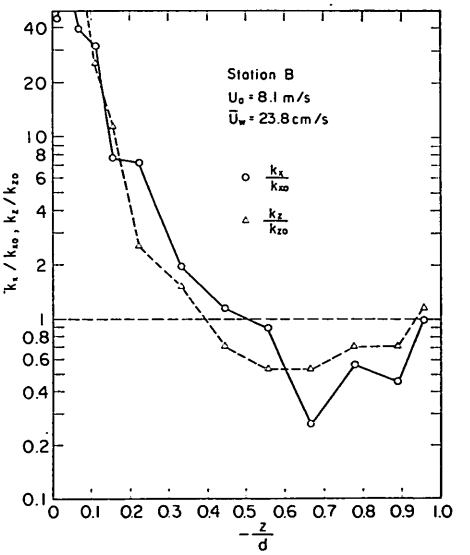


**Fig. A-10** Ratio of Adverse Wind to Current Only Eulerian Diffusion Coefficient (Station B, $\bar{U}_w = 23.8$ cm/s)

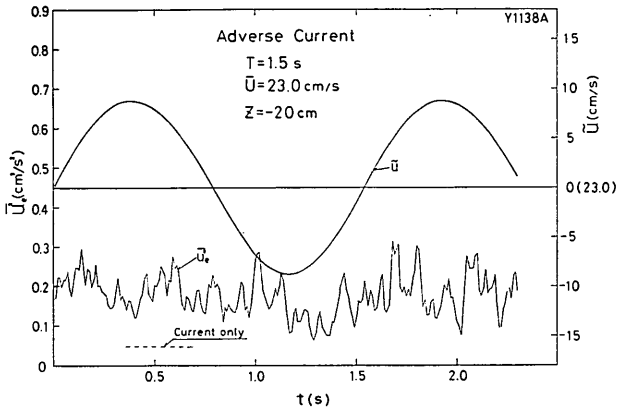


**Fig. A-11** Phase Average of Turbulence Components (Frequency Components Higher than 2Hz, $T=1.5$ s)